Turbulence and fluid-front area production in binary-species, supercritical, transitional mixing layers

N. Okong'o, and J. Bellan

Citation: Physics of Fluids **16**, 1467 (2004); doi: 10.1063/1.1688326
View online: http://dx.doi.org/10.1063/1.1688326
View Table of Contents: http://aip.scitation.org/toc/phf/16/5
Published by the American Institute of Physics

Articles you may be interested in

Subcritical to supercritical mixing
Physics of Fluids **20**, 052101 (2008); 10.1063/1.2912055

A numerical study of cryogenic fluid injection and mixing under supercritical conditions
Physics of Fluids **16**, 4248 (2004); 10.1063/1.1795011

Coupling between hydrodynamics, acoustics, and heat release in a self-excited unstable combustor
Physics of Fluids **27**, 045102 (2015); 10.1063/1.4916673

HTML ABSTRACT + LINKS

Turbulence and fluid-front area production in binary-species, supercritical, transitional mixing layers

N. Okong'o and J. Bellan
Jet Propulsion Laboratory, California Institute of Technology, Pasadena, California 91109-8099

(Received 4 March 2003; accepted 29 January 2004; published online 5 April 2004)

Databases of transitional states obtained from direct numerical simulations of temporal, supercritical mixing layers for two species systems, O_2-H_2 and $C_7H_{16}-N_2$, are analyzed to elucidate species-specific turbulence aspects and features of fluid disintegration. Although the evolution of all layers is characterized by the formation of high-density-gradient magnitude (HDGM) regions, due to the specified, smaller initial density stratification, the $C_7H_{16}-N_2$ layers display higher growth and increased global molecular mixing as well as larger turbulence levels than comparable O_2-H_2 layers. However, smaller density gradients and lower mass-fraction gradients at the transitional state for the O_2-H_2 system indicate that on a local basis, the layer exhibits an enhanced mixing, this being attributed to the increased mixture solubility and to mixture near-ideality. These thermodynamic features are found responsible for a larger irreversible entropy production (dissipation) in the O_2-H_2 compared to the $C_7H_{16}-N_2$ layers. The largest O_2-H_2 dissipation is primarily concentrated in HDGM regions that are distortions of the initial density stratification boundary, whereas the largest $C_7H_{16}-N_2$ dissipation is located in HDGM regions resulting from the mixing of the two fluids. To understand fluid disintegration, the area production of a fluid front perpendicular to the mass fraction gradient is calculated in a coordinate system moving with the relative velocity between the front and the flow. On a cross-stream local basis, the $C_7H_{16}-N_2$ layers produce more area, and area production increases with smaller perturbation wavelengths combined with larger initial Reynolds numbers. The most active area-producing layer also exhibits the largest probability of having perpendicular vorticity and mass-fraction-gradient vectors. Analysis of the terms in the area production equation shows a large pressure-gradient-term root mean square contribution for the $C_7H_{16}-N_2$ layers, due to the coincidence of regions with large magnitudes of pressure gradient with HDGM regions. Such coincidence is attributed to real-gas behavior, which is species-system specific, as the alignment of the pressure gradient and density gradient is similar for both species systems. The alignment of the mass fraction gradient with the strain rate is also species-system dependent. Independent of species system and of the initial conditions, the vorticity is preferentially aligned with the intermediate strain-rate eigendirection, indicating that eddy-viscosity-type models are not adequate for turbulent supercritical mixing. © *2004 American Institute of Physics.* [DOI: 10.1063/1.1688326]

I. INTRODUCTION

Supercritical fluids are of great interest in extraction processes as well as in propulsion devices such as liquid rockets, advanced gas-turbine and diesel engines. A substance is defined to be in a supercritical state when at a thermodynamic pressure (p) or temperature (T) exceeding the critical (subscript c) value (p_c or T_c),[1] in which state only one phase can exist;[2] the detailed explanation for the choice of this definition was provided by Harstad and Bellan.[3] Sometimes the supercritical state is defined to be in the region where the pressure and temperature are above their critical values;[4] however, there are many subtleties to the definition of the supercritical region. For a single species fluid, p_c and T_c are the maximum pressure and temperature at which two phases (liquid and vapor) may exist,[1,2] and therefore, the single phase region is well delineated ($p_r \equiv p/p_c > 1$ or $T_r \equiv T/T_c > 1$). The possible complications of retrograde condensation near the critical point[1,2] are not taken into account in this characterization. However, a binary mixture may have one or several critical loci, as shown by Prausnitz *et al.*[1] who presented at least six types or classes of binary mixtures, with five having multiple critical loci. To avoid the confusion that may be introduced for such mixtures having several critical loci, these types of mixtures are not considered; instead the focus is on simple mixtures (i.e., those having a single critical locus). The supercritical region is here defined as that for which only a single phase is possible and one in which the transport properties are generally pressure as well as temperature dependent. Since the criterion of $p_r > 1$ or $T_r > 1$ represents the thermodynamic region for which only a single phase is possible, it corresponds to our definition of the supercritical region. This definition is consistent with the utilization in the present study of a Peng–Robinson-type real gas equation of state.

In the practical situations of interest to the present study, fluid enters a chamber that is pressurized above the critical pressure of the injected fluid. The injected fluid then mixes in

 © 2004 American Institute of Physics

a highly turbulent manner with the chamber fluid and disintegrates into smaller parcels which participate in subsequent ignition and combustion. Clearly, fluid disintegration and turbulent mixing play a crucial role in determining the size and composition of the parcels of fluid, and consequently the efficiency of combustion.

Past the critical point of the fluid (where material liquid–vapor surfaces no longer exist), jet disintegration assumes the aspect of what Chehroudi *et al.*[5] call ''fingers,'' or ''comb-like structures'' at transcritical conditions, having an increasingly gaseous appearance with increasing p; these experiments were conducted with N_2-N_2, $N_2-(CO+N_2)$, $He-N_2$ and O_2-N_2. Similar experimental evidence was produced by Mayer *et al.*[6,7] for O_2 disintegration. Raman scattering measurements of the radial density in free N_2 jets at 4 MPa by Oschwald and Schik[8] showed sharp profiles independent of the injection temperature, indicating the occurrence of sharp density gradients. Regions of high density-gradient-magnitude (acronym HDGM) were also shown to exist in direct numerical simulations (DNS) of both pre-transitional[9] and transitional[10,11] supercritical binary-species mixing layers. These HDGM regions were found to be the venues for high dissipation (entropy production),[10,11] with most of the dissipation due to species-mass flux and minimal dissipation from viscous effects. The occurrence of the highest dissipation in the HDGM regions was attributed to the sharp density stratification being very effective at damping turbulent eddies,[12,13] because it is qualitatively similar to a rigid flat plate. However, there is still uncertainty as to the fundamental connection between the HDGM regions and area production during fluid disintegration.[14] In connection to fluid disintegration, area production is defined as the increase in area of fluid fronts perpendicular to the mass fraction gradient. Indeed, fluid disintegration is the formation of topologically discontinuous regions of a pure fluid of interest into another fluid, starting from a given topologically continuous volume of fluid of interest. This means that essentially the fluid of interest changes from being simply connected to being multiply connected. For a conserved fluid mass, the change from a continuously connected to discontinuous regions of fluid generally implies a change in the area of the fluid of interest. Therefore, fluid fronts perpendicular to the mass fraction gradient delineate the area created.

Relevant to studying area production are the interactions of the strain rate (S_{ij}) and vorticity (ω) with scalar fields. According to Ruetsch and Ferziger,[15] these interactions can be conceptualized as a stretch of a front of a generic scalar field G due to strain, and as a folding and wrapping of this stretched front due to the action of ω. These processes must coexist in order to affect the development of front area. Conceptually, when ω and ∇G are orthogonal, fronts become wrapped around a vortex tube, whereas when ω and ∇G are parallel, transport of the scalar increases within the front. Ruetsch and Ferziger[15] postulate that the latter situation does not lead to area production, whereas the former may lead to area production either at the front or elsewhere in the flow. A particular example of area production is flame stretching,[15–18] where the front is identified with the flame surface. Ashurst *et al.*[19] investigated the alignment of ω and passive scalar (temperature) gradient with S_{ij} under incompressible fluid conditions for both isotropic turbulence and shear flow. They found that the vorticity was most likely to point in the intermediate principal strain direction, whereas the scalar gradient was most likely to point in the most compressive (smallest) principal strain direction; the implication of their results is that vorticity and scalar gradient are most likely to be orthogonal. Ruetsch and Ferziger[15] found this to be the case for incompressible isotropic turbulence. Similar numerical results were found by Kosović *et al.*[20] for compressible turbulence. The experimental results of Tao *et al.*[21,22] confirmed these general findings. The alignment of ω and the strain rate eigenvectors was also studied by Diamessis and Nomura[23] for stably stratified, incompressible homogeneous turbulence and it was found that baroclinically generated ω acted to prevent the strain-rate axes rotation. Given that the conclusions regarding scalar gradient alignment and area production were obtained from DNS of both incompressible flows[15,19] (in which the scalar did not affect the dynamic field) and atmospheric-pressure compressible flows,[20] it is pertinent to inquire whether they are valid at high-pressure. Supercritical mixing layers (in which the HDGM influence the turbulence) offer such a situation.

TABLE I. Pure species properties; v_c is the molar volume at the critical point.

Species	m (g/mol)	T_c (K)	p_c (MPa)	v_c (cm^3/mol)
H_2	2.016	33.0	1.284	64.3
N_2	28.013	126.3	3.399	89.8
O_2	31.999	154.6	5.043	73.4
C_7H_{16}	100.205	540.2	2.74	432.0

In this paper, we undertake an analysis of supercritical binary-species mixing layers, leading to insights into turbulence and fluid-front area production under supercritical conditions. The DNS database, described in detail elsewhere,[9–11] consists of two very different binary species systems, $C_7H_{16}-N_2$ and O_2-H_2. The properties of these species are listed in Table I. The $C_7H_{16}-N_2$ represents the hydrocarbon–air system found in gas-turbine and diesel engines, which is currently too complex for detailed fundamental simulations, while the O_2-H_2 system is relevant to liquid rockets; a comparison of these two systems has already been performed in the realm of drop behavior[24] and for the similarity solution of a temporal mixing layer,[25] but was restricted to laminar flows. The mixing layers have initially a strong density stratification between the two free streams, each of which is composed of a single species. The layers are initially perturbed to enhance their growth and structure formation, leading to their evolution to a transitional state. For each species system, several simulations were performed with various initial conditions.

This paper is organized as follows: In Sec. II, we briefly recall the DNS methodology, including conservation equations, equation of state, transport properties, initial and boundary conditions and numerical scheme. We then discuss the choice of initial conditions for meaningful comparisons

between results obtained for the two species systems, given their differing thermodynamics. Section III contains the results, encompassing the investigation of the global layer characteristics, the scrutiny of the HDGM regions, the specifics of the irreversible entropy production and its relationship to the HDGM regions, and the exploration of the mechanisms leading to fluid-front area production for fronts perpendicular to the mass fraction gradient. Finally, in Sec. IV, the results are summarized and conclusions are presented.

II. DNS EQUATIONS AND METHODOLOGY

A detailed description of the DNS methodology has been given by Miller *et al.*[9] and Okong'o and Bellan[10] for $C_7H_{16}-N_2$ layers and by Okong'o *et al.*[11] for the O_2-H_2 layers. Those descriptions are summarized here to emphasize aspects of the formulation that are different from the typical low-pressure situation. These flows are density stratified but gravitational effects are neglected. The DNS governing equations consist of conservation equations, the equation of state (EOS) and transport property relations, which are solved for specific initial and boundary conditions using a suitably accurate numerical scheme.

A. Conservation equations

The conservation equations originate in Keizer's[26] fluctuation-dissipation theory which is consistent with nonequilibrium thermodynamics, converges to kinetic theory in the low-pressure limit and relates fluxes and forces from first principles. For a binary mixture, the conservation equations are

$$\frac{\partial \rho}{\partial t}+\frac{\partial(\rho u_i)}{\partial x_i}=0, \tag{1}$$

$$\frac{\partial(\rho u_i)}{\partial t}+\frac{\partial(\rho u_i u_j+p\,\delta_{ij})}{\partial x_j}=\frac{\partial \tau_{ij}}{\partial x_j}, \tag{2}$$

$$\frac{\partial(\rho Y_\alpha)}{\partial t}+\frac{\partial(\rho Y_\alpha u_i)}{\partial x_i}=-\frac{\partial j_{\alpha i}}{\partial x_i}, \quad \alpha=1,N, \tag{3}$$

$$\frac{\partial(\rho e_t)}{\partial t}+\frac{\partial[(\rho e_t+p)u_i]}{\partial x_i}=-\frac{\partial q_{\mathrm{IK}i}}{\partial x_i}+\frac{\partial \tau_{ij}u_j}{\partial x_i}, \tag{4}$$

where x is a Cartesian coordinate, t is time, ρ is the density, u_i is the ith component of the velocity, $e_t=e+u_iu_i/2$ is the total energy (i.e., internal energy, e, plus kinetic energy), Y_α is the mass fraction of species α and $\mathbf{j}_\alpha$ is its mass flux vector ($\Sigma_{\alpha=1}^N Y_\alpha=1$, $\Sigma_{\alpha=1}^N j_{\alpha i}=0$) for a mixture of N species. In the binary ($N=2$) mixing layer configuration, the lighter (molar weight) species (subscript 1) is in the upper stream, and the other species (subscript 2) is in the lower stream. Furthermore, $\mathbf{q}_{\mathrm{IK}}$ is the Irwing–Kirkwood (subscript IK) form of the heat flux vector (see Sarman and Evans),[27] and τ_{ij} is the Newtonian viscous stress tensor

$$\tau_{ij}=2\mu(S_{ij}-\tfrac{1}{3}S_{kk}\delta_{ij}), \tag{5}$$

where the strain rate is

$$S_{ij}=\frac{1}{2}\left(\frac{\partial u_i}{\partial x_j}+\frac{\partial u_j}{\partial x_i}\right), \tag{6}$$

δ_{ij} is the Kronecker delta function, and μ is the mixture viscosity that is in general a function of the thermodynamic state variables. The mass flux and heat flux are given by

$$j_{2i}=-\left[j'_{2i}+(\alpha_{\mathrm{IK}}-\alpha_h)Y_2Y_1\frac{\rho D}{T}\frac{\partial T}{\partial x_i}\right], \tag{7}$$

$$q_{\mathrm{IK}i}=-\kappa'_{\mathrm{IK}}\frac{\partial T}{\partial x_i}-\alpha_{\mathrm{IK}}R_uT\frac{m}{m_2m_1}j'_{2i}, \tag{8}$$

$$j'_{2i}=\rho D\left[\alpha_D\frac{\partial Y_2}{\partial x_i}+\frac{Y_2Y_1}{R_uT}\frac{m_2m_1}{m}\left(\frac{v_{,2}}{m_2}-\frac{v_{,1}}{m_1}\right)\frac{\partial p}{\partial x_i}\right], \tag{9}$$

$$\alpha_h=\frac{1}{R_uT}\frac{m_2m_1}{m}\left(\frac{h_{,2}}{m_2}-\frac{h_{,1}}{m_1}\right). \tag{10}$$

The notation in Eqs. (7)–(10) is as follows: D is the binary diffusion coefficient; α_D is the mass diffusion factor ($\alpha_D=1$ for an ideal mixture); m_α is the molar mass of species α; $m=\Sigma_{\alpha=1}^N m_\alpha X_\alpha$ is the mixture molar mass where the molar fraction $X_\alpha=mY_\alpha/m_\alpha$; $v_{,\alpha}=(\partial v/\partial X_\alpha)_{T,p,X_{\beta(\beta\neq\alpha)}}$ is the partial molar volume and $h_{,\alpha}=(\partial h/\partial X_\alpha)_{T,p,X_{\beta(\beta\neq\alpha)}}$ is the partial molar enthalpy; $v=\Sigma_{\alpha=1}^N X_\alpha v_{,\alpha}$ is the molar volume related to the density by $v=m/\rho$; $h=\Sigma_{\alpha=1}^N X_\alpha h_{,\alpha}$ is the molar enthalpy; R_u is the universal gas constant and κ'_{IK} is a thermal conductivity defined from the transport matrix through

$$\kappa'_{\mathrm{IK}}=\kappa+X_1X_2\alpha_{\mathrm{IK}}\alpha_{\mathrm{BK}}R_u\rho D/m, \tag{11}$$

with $\lim_{p\to 0}\kappa=\kappa_{\mathrm{KT}}$ as discussed in Harstad and Bellan,[28] where the subscript KT refers to Kinetic Theory. The transport coefficients associated with the Soret (in the molar fluxes) and the Dufour (in the heat flux) terms of the transport matrix are α_{BK} and α_{IK}, which are two forms of the thermal diffusion factor corresponding to the IK and the Bearman–Kirkwood (subscript BK) forms of the heat flux (see Sarman and Evans),[27] respectively. These transport coefficients are characteristic of each particular species pairs and they obey the relationship[28]

$$\alpha_{\mathrm{BK}}=\alpha_{\mathrm{IK}}-\alpha_h. \tag{12}$$

Additionally, $\lim_{p\to 0}\alpha_{\mathrm{IK}}\neq\alpha_{\mathrm{KT}}$ and $\lim_{p\to 0}\alpha_{\mathrm{BK}}=\alpha_{\mathrm{KT}}$.

B. Equation of state

The pressure is calculated from the well-known Peng–Robinson (PR) EOS, given T and the PR molar volume (v_{PR}), as

$$p=\frac{R_uT}{(v_{\mathrm{PR}}-b_m)}-\frac{a_m}{(v_{\mathrm{PR}}^2+2b_mv_{\mathrm{PR}}-b_m^2)}, \tag{13}$$

where a_m and b_m are functions of T and X_α. At high pressures, v_{PR} may differ significantly from the actual molar volume v,[1] which naturally introduces the volume shift $v_S\equiv v-v_{\mathrm{PR}}$. Both v_{PR} and v_S can be calculated from the PR EOS given p, T, and X_α,[29] although for the $C_7H_{16}-N_2$ system v_S is negligible. All thermodynamic quantities, including α_D, h,

TABLE II. Transport properties for binary mixtures. The reference temperature is $T_R=(T_1+T_2)/2$, T in Kelvin; Y_O is the O_2 mass fraction, Y_h is the C_7H_{16} mass fraction.

System	$C_7H_{16}-N_2$	O_2-H_2
$\mu=\mu_R(T/T_R)^n$	$n=0.7$	$n=0.75$
$Sc\equiv\mu/(\rho\alpha_D D)$	$1.5-Y_h$	$(1.334-0.668Y_O-0.186Y_O^2-0.268Y_O^6)[1+(88.6/T)^{1.5}]$
$\Pr\equiv\mu C_p/(m\kappa)$	$0.5\mathrm{Sc}/\exp(-1.5Y_h)$	$1.335/T^{0.1}$
α_{IK} or α_{BK}	$\alpha_{IK}=0.1$ (Ref. 28)	$\alpha_{BK}=0.2$ (Refs. 30 and 31)
T range	500–1100 K	200–800 K
p range	40–80 atm	~100 atm

$C_p=(\partial h/\partial T)_{p,X}$ and the speed of sound (a_s), are calculated from the EOS using standard thermodynamic relations.[9–11] The calculation of p and T from the known conservative variables of Eqs. (1)–(4) uses an iterative scheme[11] for O_2-H_2 and an energy fit[10] for $C_7H_{16}-N_2$.

C. Transport coefficients

The viscosity, the Schmidt number (Sc) and the Prandtl number (Pr) were calculated from high-pressure single-species transport properties using mixing rules, as in Harstad and Bellan.[30] The calculated values were correlated, as summarized in Table II, and these correlations were then used to compute the transport properties D and κ. The temperatures T_1 (upper, H_2 or N_2, stream) and T_2 (lower, O_2 or C_7H_{16}, stream) in Table II correspond to the free-stream temperatures for mixing layer simulations. The value of the reference viscosity (μ_R) is determined by the specified value of the initial Reynolds number Re_0 [see Eq. (16)], chosen so as to enable the resolution of all relevant length scales. One of the forms of the thermal diffusion factor is specified and the other form is calculated from Eq. (12).

D. Configuration, initial and boundary conditions

The temporally developing mixing layer configuration is depicted in Fig. 1 for O_2-H_2, as an example, showing the definition of the streamwise (x_1), cross-stream (x_2) and spanwise (x_3) coordinates. The layer is not symmetric in extent in the x_2 direction so as to accommodate the larger layer growth in the lighter fluid (H_2 or N_2) side. The free-stream density (ρ_1 or ρ_2) is calculated for each pure species at its free-stream temperature (T_1 or T_2) and at the initial uniform pressure (p_0). The vorticity thickness is defined as $\delta_\omega(t)=\Delta U_0/(\partial\langle u_1\rangle/\partial x_2)_{\max}$ where $\langle u_1\rangle$ is the (x_1,x_3) planar average of the streamwise velocity, and $\Delta U_0=U_1-U_2$ is the velocity difference across the layer. The simulation is initiated with four spanwise vortices, which pair twice to produce an ultimate vortex. The choice

$$U_1=2M_{c,0}a_{s_1}\left[1+\left(\frac{a_{s_1}}{a_{s_2}}\right)\sqrt{\frac{\rho_1 Z_1}{\rho_2 Z_2}}\right]^{-1},\qquad U_2=-\sqrt{\frac{\rho_1 Z_1}{\rho_2 Z_2}}U_1, \tag{14}$$

was made with the intent of keeping the ultimate vortex stationary in the computational domain,[9] although the relations of Papamoschou and Roshko[32]

$$U_1=2M_{c,0}a_{s_1}\left[1+\left(\frac{a_{s_1}}{a_{s_2}}\right)\sqrt{\frac{\rho_1}{\rho_2}}\right]^{-1},\quad U_2=-\sqrt{\frac{\rho_1}{\rho_2}}U_1, \tag{15}$$

were also used for some simulations reported here. Here $M_{c,0}$ is the convective Mach number and $Z=p/(\rho TR_u/m)$ is the compression factor indicating departures from perfect gas ($Z=1$) behavior. The specification of $M_{c,0}$, therefore, determines ΔU_0. Given the initial streamwise velocity profile u_1 based on U_1 and U_2, $(\partial\langle u_1\rangle/\partial x_2)_{\max}$ and hence $\delta_{\omega,0}\equiv\delta_\omega(0)$ are calculated. The specified value of the initial flow Reynolds number,

$$\mathrm{Re}_0=\frac{0.5(\rho_1+\rho_2)\Delta U_0\delta_{\omega,0}}{\mu_R}, \tag{16}$$

is then used to calculate μ_R.

The simulations are started with error-function profiles for the mean streamwise velocity, mass fraction and temperature, upon which are imposed spanwise and streamwise vorticity perturbations[33,34] of amplitudes F_{2D} and F_{3D}, respectively, whose streamwise (λ_1) and spanwise (λ_3) wavelengths are $\lambda_1=C\delta_{\omega,0}$ and $\lambda_3=0.6\lambda_1$, where $C=7.29$ is the most unstable wavelength for incompressible flow. For some simulations reported here, other values of C obtained from stability analyses[25] were also used: $C=10.35$ or 10.61 for the most unstable wavelength for the O_2-H_2 layer (depending on the initial conditions) and $C=4.57$ for the short-

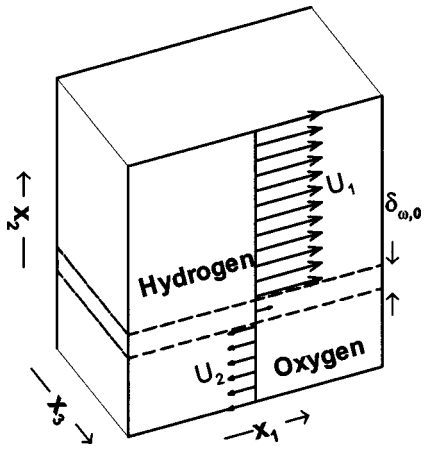

FIG. 1. Sketch of the O_2-H_2 mixing layer configuration.

TABLE III. Mean flow properties for various mixing layers; $M_{c,0}=0.4$.

	$\rho_2/\rho_1=12.88$		$\rho_2/\rho_1=24.40$		$\rho_2/\rho_1=24.51$	
Stream	C_7H_{16}	N_2	O_2	H_2	O_2	H_2
u_1 (m/s)	−85.947	209.856	−158.004	770.983	−114.926	568.972
a_s (m/s)	181.327	643.709	397.517	1915.376	295.985	1381.95
ρ (kg/m^3)	259.487	20.141	96.764	3.965	197.317	8.050
p_0 (atm)	60	60	100	100	100	100
T (K)	600	1000	400	600	235	287
Y_2	1	0	1	0	1	0
Z	0.4706	1.017	1.008	1.033	0.841	1.063
$p_r=p/p_c$	2.22	1.81	2.01	7.89	2.01	7.89
$\Delta U_0=U_1-U_2$	295.80		928.99		683.90	
$\lvert\rho_2U_2\rvert/\lvert\rho_1U_1\rvert$	5.276		5.001		4.951	

est (estimated) unstable wavelength for the $C_7H_{16}-N_2$ layer. The grid is chosen for all simulations so as to accommodate four wavelengths in the streamwise and spanwise directions, and the evolution of the layer is meant to encompass roll-up and two pairings of the initial spanwise vortices.

The boundary conditions are periodic in the streamwise and spanwise directions, and of outflow type for real gas in the cross-stream direction, as derived by Okong'o and Bellan.[35] The outflow type conditions are essential to maintain numerical stability since the initial perturbation causes large pressure waves that must be allowed out of the domain with minimal reflection.

E. Numerics

The conservation equations were numerically solved using a fourth-order explicit Runge–Kutta time integration and a sixth-order compact scheme with eighth-order filter for spatial derivatives;[36] for numerical stability, filtering is applied at interior points only. The computations were parallelized using three-dimensional domain decomposition and message passing, and an efficient parallel tridiagonal solver.[37]

F. Free-stream conditions

The intent is here to compare results from DNS for the $C_7H_{16}-N_2$ and O_2-H_2 systems in order to elucidate species-system-specific turbulence aspects. Meaningful comparisons require that the initial conditions be matched in ways to be determined. The thermodynamic initial conditions (p_0, T_1, T_2) are chosen for the $C_7H_{16}-N_2$ system to be in the regime of relevance to gas turbine and diesel engines (60 atm, $T_1=1000$ K, $T_2=600$ K), whereas those for the O_2-H_2 system are selected as close to the liquid rocket conditions as computationally feasible (100 atm, $T_1=600$ K, $T_2=400$ K or 100 atm, $T_1=287$ K, $T_2=235$ K) because the quite different thermodynamic properties of the two mixtures (as encapsulated by their respective equations of state) do not permit the matching of the thermodynamic initial conditions (see discussion in Ref. 11). These three sets of free stream conditions, listed in Table III, have quite similar momentum ratios $\lvert\rho_2U_2\rvert/\lvert\rho_1U_1\rvert$, and the initial pressure is such that the reduced pressure $(p_r\equiv p/p_c)$ in the heavier fluids is similar. However, p_r is dissimilar for the lighter fluids. Attempting a larger temperature difference between the two free streams of the O_2-H_2 layers, in order to match the reduced temperature $(T_r\equiv T/T_c)$ or the dimensionless temperature difference $(\lvert T_2-T_1\rvert/T_2)$ of the $C_7H_{16}-N_2$ layers, leads to an excessively large density stratification, as illustrated in Fig. 2(a) which shows ρ_2/ρ_1 over a range of T_1 and T_2 at $p=100$ and 400 atm.

The effect of the density stratification on the stability of the layer has been investigated using two-dimensional (x_1, x_2) inviscid stability analyses based on the error function mean profiles.[25] The stability curves for the layers in Table III, duplicated from Ref. 25, are plotted in Fig. 2(b).

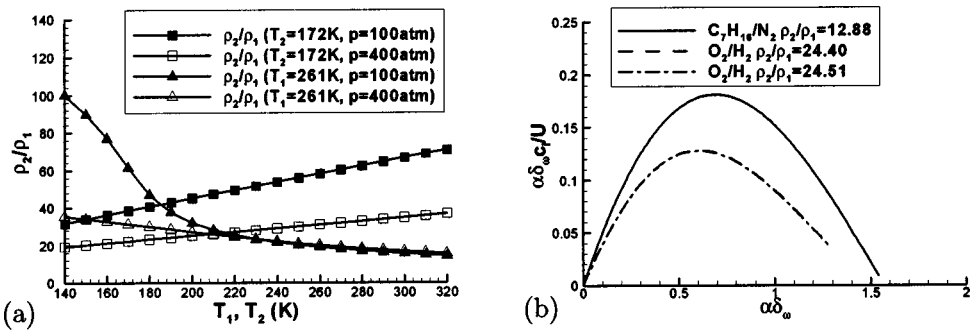

FIG. 2. (a) ρ_2/ρ_1 vs T_1 and T_2 for O_2-H_2 at different conditions; (b) comparison of the stability curves for $C_7H_{16}-N_2$ and O_2-H_2 layers in Table III. [Note: In (b), the O_2-H_2 curves overlap.]

TABLE IV. Listing of the simulations and associated resolution for O_2-H_2 (OH) and $C_7H_{16}-N_2$ (HN) mixing layers. L_i is the size of the domain in the x_i direction, in meters. For all layers, $L_1=4\lambda_1$, $\delta_{\omega,0}=6.859\times10^{-3}$ m and $F_{2D}=0.1$. The other initial conditions are listed in Table III under the value of ρ_2/ρ_1. The subscript tr denotes the transitional time. The CPU time is based on an SGI Origin2000 300 MHz R12000 processor.

Run	Re_0	ρ_2/ρ_1	$\lambda_1/\delta_{\omega,0}$	F_{3D}	$L_1\times L_2\times L_3$	$N_1\times N_2\times N_3$	$Re_{m,tr}$	t^*_{tr}	CPU(h)
OH500	500	24.51	10.61	0.025	0.291×0.291×0.1746	352×352×208	1772	290	14557
OH550	550	24.40	10.35	0.025	0.284×0.284×0.17	352×352×208	1907	270	14497
OH750	750	24.40	7.29	0.05	0.2×0.2×0.12	352×352×208	1507	150	10349
HN500	500	12.88	7.29	0.05	0.2×0.232×0.12	240×288×144	1250	155	1714
HN600	600	12.88	7.29	0.05	0.2×0.232×0.12	288×336×176	1452	135	5156
HN800	800	12.88	4.57	0.05	0.125×0.148×0.075	240×272×144	1258	100	1916

The increased stability of the O_2-H_2 layers is mainly due to their higher density stratification.

III. RESULTS

Previously performed DNS for the free-stream conditions displayed in Table III are studied here and their initial conditions are listed in Table IV. Details of the computations, including the adequacy of the resolution, are discussed in Refs. 10 and 11. Due to the higher initial density stratification for O_2-H_2 (OH) layers compared to $C_7H_{16}-N_2$ (HN), an O_2-H_2 layer with same dynamic initial conditions as HN600, including $Re_0=600$, did not reach transition and thus it is not possible to compare transitional results for the two species systems when $Re_0=600$. Transition was determined by an ensemble of criteria, in that it was necessary to obtain a peak of global-averaged positive spanwise vorticity (used as a measure of the small-scale activity) after the second pairing, in conjunction with smooth one-dimensional energy spectra indicating loss of memory of the initial condition and a peak in or continued increase of momentum thickness.

Considering the dynamic and thermodynamic initial conditions, several types of comparisons are meaningful, as follows: (1) Layers OH750 and HN600 have the same dynamic initial conditions $\lambda_1/\delta_{\omega,0}$ and F_{3D}, and achieve similar momentum-thickness-based Reynolds number, $Re_m=Re_0\,\delta_m/\delta_{\omega,0}$ [see definition of δ_m in Eq. (17)], at transition, $Re_{m,tr}$. However, they represent different species systems and have different initial conditions for ρ_2/ρ_1, T_1 and T_2. (2) Layers HN500 and HN800 represent the same species system, have the same initial ρ_2/ρ_1, F_{3D} and achieve similar $Re_{m,tr}$. However, they are initially perturbed at different $\lambda_1/\delta_{\omega,0}$. (3) Layers OH500 and HN500 have the same Re_0, but they represent different species systems and have different ρ_2/ρ_1, $\lambda_1/\delta_{\omega,0}$, F_{3D}, T_1 and T_2. (4) Layers OH500 and OH550 represent the same species system, have similar ρ_2/ρ_1, F_{3D} and Re_0, and are both excited at the most unstable wavelength obtained from the compressible stability analysis; however, they have different T_1 and T_2. Each of these four comparisons should elucidate the effect of some initial conditions and concerted consideration of all these results should indicate which of these parameters most influence turbulence and area production. Since OH and HN follow different real gas EOS, the distinction between the effects of density, composition and temperature variations cannot made as it could be if both mixtures were perfect gases; for example, a single species real gas at constant pressure does not obey the perfect gas relation $\rho_2/\rho_1=T_1/T_2$.

We note here that for a mixture, T_c and p_c depend on composition and are different from the pure species values. For the OH and HN mixtures, whereas the local T_c is between the pure species values, the local p_c may exceed the individual species p_c (e.g., for HN, see Ref. 10, $T_{c,\max}=540$ K and $p_{c,\max}>8000$ atm). Although all layers are at supercritical temperature, it is found[10] that whereas the free streams are at supercritical pressure, the mixing layer is at subcritical pressure; therefore, by the definition stated in the Introduction, all layers are supercritical at every point in space and time, regardless of the instantaneous composition. The O_2-H_2 layers are close to perfect gases and ideal mixtures,[11] while the $C_7H_{16}-N_2$ layers have significant real gas and mixture non-ideality effects[10] (see also Z in Table III); both mixtures were consistently modeled in that the mixture-specific EOS, Sc, Pr, mixture nonideality and Soret and Dufour effects (thermal diffusion) were retained for thermodynamic consistency in real gas behavior. Analysis of the simplified governing equations, which yielded similarity solutions,[25] revealed profound differences between the mean flow profiles of perfect gases compared to those of real gases, therefore, it is to be expected that the turbulence characteristics will also be dissimilar.

A. Global growth and rotational characteristics

A fundamental characteristic of mixing layers is their growth. Although many definitions of growth exist, Cortesi *et al.*[38] showed that several such measures, including the momentum thickness, are qualitatively similar. Here, we define the momentum thickness as

$$\delta_m=\frac{1}{(\theta_1-\theta_2)^2}\int_{L_{2,\min}}^{L_{2,\max}}(\theta_2-\langle\rho u_1\rangle)(\theta_1-\langle\rho u_1\rangle)dx_2, \tag{17}$$

with $\theta_1=\langle\rho u_1\rangle_{x_2=L_{2,\max}}$ and $\theta_2=\langle\rho u_1\rangle_{x_2=L_{2,\min}}$, where $L_{2,\min}=-L_2/3$ and $L_{2,\max}=2L_2/3$ and L_2 is the cross-stream extent of the computational domain. While the growth is mostly a consequence of entrainment, the product thickness defined as $\delta_p=\int\int\int_V\rho Y_p dV$ in mass units, where $Y_p=2\min(Y_1,Y_2)$, is a direct consequence of molecular mixing as also explained by Cortesi *et al.*[38] $\delta_m/\delta_{\omega,0}$ is illustrated as a function of the nondimensional time $t^*=t\Delta U_0/\delta_{\omega,0}$ in Fig. 3(a) for all simulations. All layers roll up and pair twice,

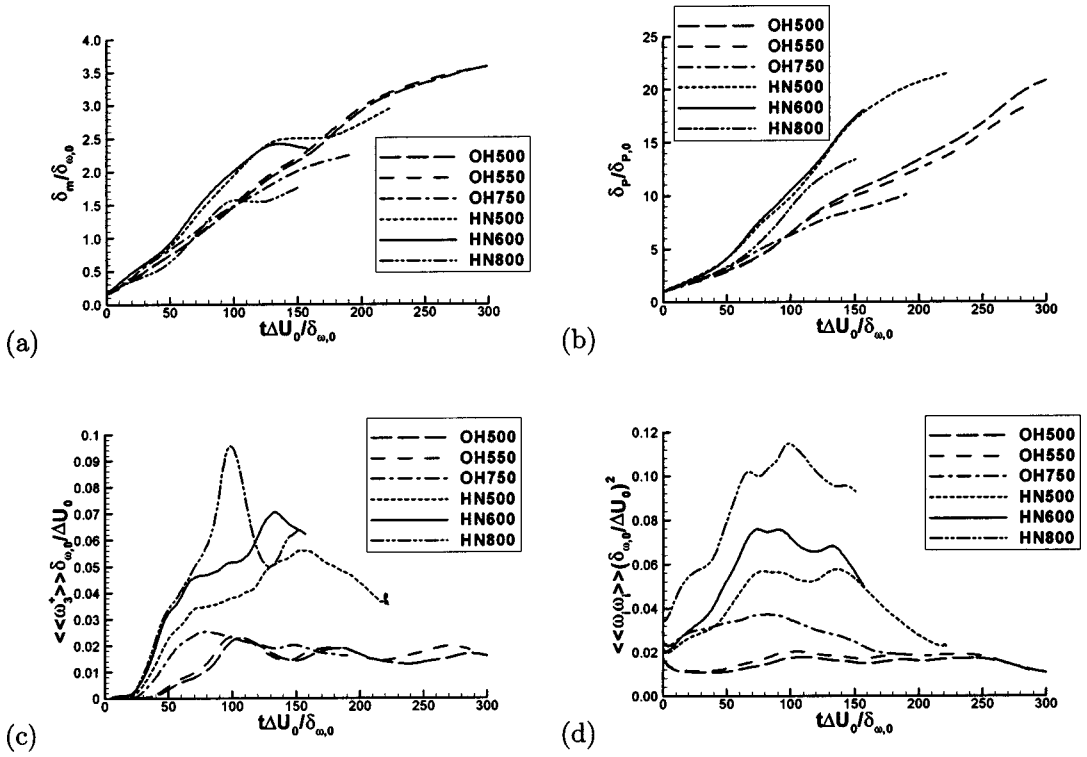

FIG. 3. Nondimensionalized (a) momentum thickness, (b) product thickness, (c) global positive spanwise vorticity, and (d) enstrophy, all vs $t^* = t/(\Delta U_0/\delta_{\omega,0})$.

however, the $C_7H_{16}-N_2$ layers display a drastic increase in $\delta_m/\delta_{\omega,0}$ after the first pairing, whereas their O_2-H_2 counterpart tend to grow more slowly. The drastic growth of the $C_7H_{16}-N_2$ layers compared to the O_2-H_2 ones is attributed to the smaller initial density stratification of the former. This is also the reason that the $C_7H_{16}-N_2$ layers exhibit a plateau after the second pairing, this being a manifestation of forcing; no such effect is discernible for the more highly-density-stratified O_2-H_2 layers, which are more resistant to entrainment and seem to grow more linearly. Not surprisingly, $\delta_p/\delta_{p,0}$, depicted in Fig. 3(b) displays a much larger growth for $C_7H_{16}-N_2$ than for O_2-H_2 as a function of t^*, meaning that global molecular mixing is much more intense.

Illustrated in Fig. 3(c) is the nondimensional positive spanwise vorticity, $\langle\langle\omega_3^+\rangle\rangle(\delta_{\omega,0}/\Delta U_0)$, which is indicative of small turbulent scale formation considering that due to the initial mean velocity profile, the initial spanwise vorticity is negative. The nondimensional enstrophy, $\langle\langle\omega_i\omega_i\rangle\rangle(\delta_{\omega,0}/\Delta U_0)^2$, where $\langle\langle\ \rangle\rangle$ denotes volume averaging, is shown in Fig. 3(d) and is a manifestation of stretching and tilting, which is the mechanism primarily responsible for the formation of small scales. For all simulations, $\langle\langle\omega_3^+\rangle\rangle(\delta_{\omega,0}/\Delta U_0)$ increases from the null value once the layer roll-up is completed; for each of the set of species, the layer perturbed at the shortest wavelength exhibits the earliest roll-up and highest $\langle\langle\omega_3^+\rangle\rangle(\delta_{\omega,0}/\Delta U_0)$ maximum growth. Noticeably, the two O_2-H_2 layers perturbed at the most unstable wavelength and having a smaller Re_0 display a delayed roll-up with respect to all other layers. Comparing the O_2-H_2 and $C_7H_{16}-N_2$ layers, one observes a drastically reduced $\langle\langle\omega_3^+\rangle\rangle(\delta_{\omega,0}/\Delta U_0)$ augmentation rate for the former compared to the latter (with particular significance for the OH500 and HN500 layers, which have the same Re_0) indicating a reduced layer growth rate. All curves exhibit local peaks at the first pairing; however, $\langle\langle\omega_3^+\rangle\rangle(\delta_{\omega,0}/\Delta U_0)$ increases following the first pairing of the $C_7H_{16}-N_2$ layers but decreases for the O_2-H_2 layers. Moreover, $\langle\langle\omega_3^+\rangle\rangle(\delta_{\omega,0}/\Delta U_0)$ is considerably smaller for the O_2-H_2 layer compared to the equivalent $C_7H_{16}-N_2$ ones, indicating that turbulence for the former is substantially reduced with respect to the latter. The enstrophy variation is consistent with this physical picture, displaying reduced levels for the O_2-H_2 layers when compared to the $C_7H_{16}-N_2$ ones. The largest enstrophy among O_2-H_2 layers corresponds to the one exhibiting the earliest roll-up and maximum positive spanwise vorticity.

Details of the turbulence and mixing characteristics at the layer transitional states will be characterized through flow visualizations as well as investigations of the irreversible entropy production and of the area production.

B. Flow visualizations at transition

The dynamical characteristics of the layers are further analyzed through the spanwise vorticity, shown in Fig. 4 for the layers listed in Table IV, in the braid planes at the respective transitional times. All contour plots depict only the significant portion of the computational domain in the x_2 direction. The creation of positive spanwise vorticity, plotted in solid lines, implies small scale production. Important qualitative differences among the layers are apparent. In addition to the vorticity magnitude being lower for O_2-H_2 layers, as previously seen from the global measures, the char-

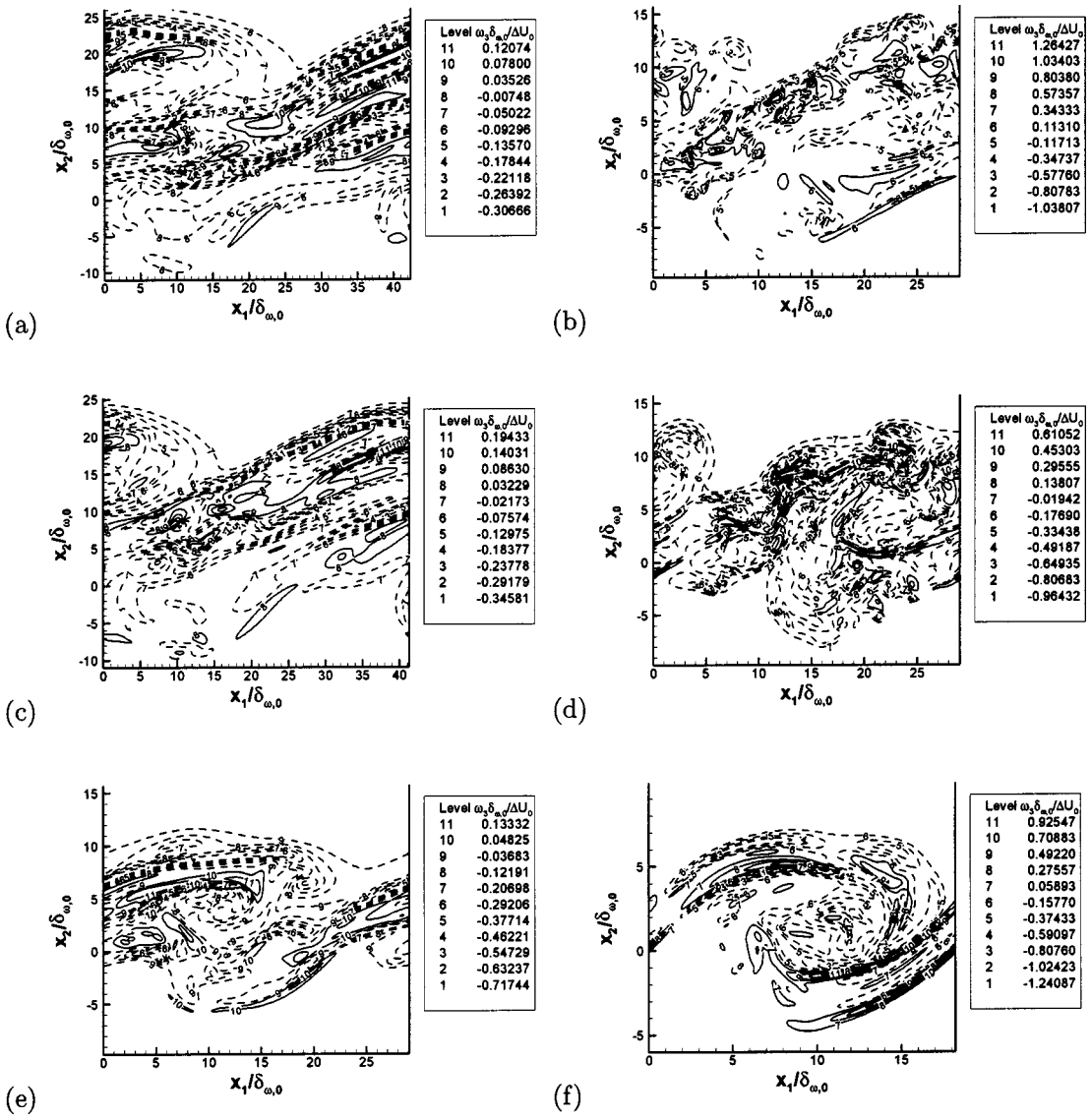

FIG. 4. Spanwise vorticity for (a) OH500, (b) HN500, (c) OH550, (d) HN600, (e) OH750, and (f) HN800: In the braid plane ($x_3 = L_3/16$). Dashed lines denote negative values.

acteristic scales over which changes in the vorticity occur are evidently larger for the O_2-H_2 layers compared to their $C_7H_{16}-N_2$ counterpart. These larger length scales are attributed to the differences in species-system thermodynamics, as discussed below. The HN800 layer [Fig. 4(f)] displays a qualitatively smooth aspect in that the ultimate vortex is not much distorted, whereas both the HN500 and HN600 layers [Figs. 4(b) and 4(d)] show a highly distorted ultimate vortex. Detailed analysis of the ω_3 budget for HN500 and HN600 carried out elsewhere[10] revealed that the stretching term dominated vorticity production as a result of small scale formation proceeding concomitant with entrainment. A detailed examination of contour plots at different time stations reveals that for HN800, the evolution of the small scales is delayed with respect to entrainment, thus leading to its smooth aspect despite the attainment of transition. The OH layers, in which small scale production is also delayed with respect to entrainment, display a rather smooth aspect that is more similar to HN800 than to the other HN layers. The different characteristics of the OH and HN layers are further examined below and shown to originate in the different thermodynamic properties of the mixtures.

As previously mentioned, HDGM regions are a distinctive feature of supercritical mixing layers and supercritical jets.[5,8] Movie animations of the $|\nabla\rho|$ timewise evolution show that the origin of these regions is not only from the distortion of the initial boundary between the two species, but also from their mixing; this conclusion holds independent of the binary system of species. Also independent of the species system is the observation that the upper stream HDGM regions mostly originate from the mixing of the species, whereas the lower stream HDGM regions mostly stem from the distortion of the initial boundary between the two species. Depicted in Fig. 5 is $|\nabla\rho|\delta_{\omega,0}/\Delta\rho_0$ in the same planes and at the same times as those in Fig. 4; the $|\nabla\rho|\delta_{\omega,0}/\Delta\rho_0$ contour levels range from 10% to 90% of the highest value in the domain. Species-system-dependent aspects can be discerned by comparing HN600 [Fig. 5(d)] and

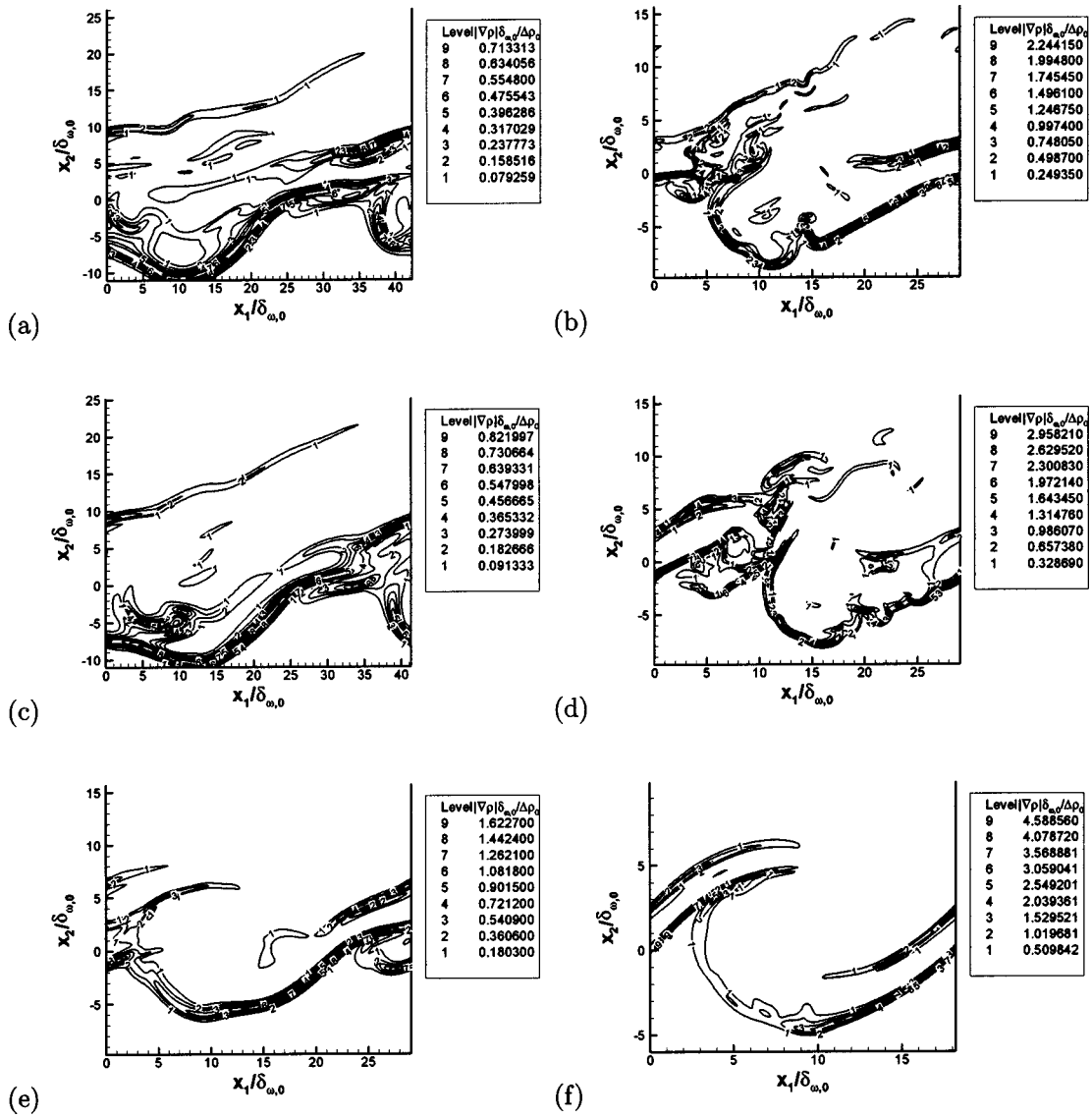

FIG. 5. Density gradient magnitude for (a) OH500, (b) HN500, (c) OH550, (d) HN600, (e) OH750, and (f) HN800: In the braid plane ($x_3 = L_3/16$).

OH750 [Fig. 5(e)], which have a similar magnitude of $\mathrm{Re}_{m,tr}$ and are excited with the same $\lambda_1/\delta_{\omega,0}$ and F_{3D} (see Table IV). Although the OH750 layer is initiated with about the same $|\nabla\rho|\delta_{\omega,0}/\Delta\rho_0$ value (albeit with about twice the density stratification) of HN600, $|\nabla\rho|\delta_{\omega,0}/\Delta\rho_0$ at transition is about a factor of 2 smaller than that of HN600. The larger $|\nabla\rho|\delta_{\omega,0}/\Delta\rho_0$ value for the HN600 layer is due to the increased nonideality of the $C_7H_{16}-N_2$ mixture (i.e., $0.5<\alpha_D<1$),[10] which impedes molecular mixing when compared to the O_2-H_2 mixture (i.e., $\alpha_D\sim 1$).[11] Independent of the initial conditions, individual HDGM regions in the O_2-H_2 layers exhibit a greater spatial extent than their $C_7H_{16}-N_2$ counterpart, which results from the combined effect of the much larger solubility of H_2 into O_2 than of N_2 into C_7H_{16} and of the much better molecular mixing of O_2-H_2. Thus, nonideality manifests itself both through increased value of $|\nabla\rho|\delta_{\omega,0}/\Delta\rho_0$ (labeled "stronger" HDGM regions) and through narrower individual HDGM regions. Comparing the other layers in Fig. 5, it is apparent that $|\nabla\rho|\delta_{\omega,0}/\Delta\rho_0$ increases with Re_0 at otherwise similar initial conditions (HN500 versus HN600; OH500 versus OH550). For same $C_7H_{16}-N_2$ initial conditions (HN500 versus HN600), the HDGM regions are distributed over a larger portion of the domain with increasing Re_0. The much larger $|\nabla\rho|\delta_{\omega,0}/\Delta\rho_0$ values of the HN800 layer are attributed to the decreased characteristic time of the flow, induced by the larger Re_0, which leads to a reduced ratio of the distortion time to the molecular mixing time. The more convoluted structure of the HN500 layer compared to the HN800 layer, despite being the same species at similar $\mathrm{Re}_{m,tr}$, results from the relative ease in distorting the weaker HDGM regions in the former simulation. This explanation is consistent with the experimental observations of Hannoun *et al.*[12] who showed that strong HDGM regions tend to act akin to a solid wall, damping turbulence and are, therefore, not easily distorted.

Species-dependent mixing attributes are also evident from contour plots of Y_2 presented in Fig. 6 and of $|\zeta|$, where $\zeta \equiv \nabla Y_2$, presented in Fig. 7, in the same planes and at the same times as those in Figs. 4 and 5. Figure 6 shows that for all mixing layers, the mixing region coincides with the ulti-

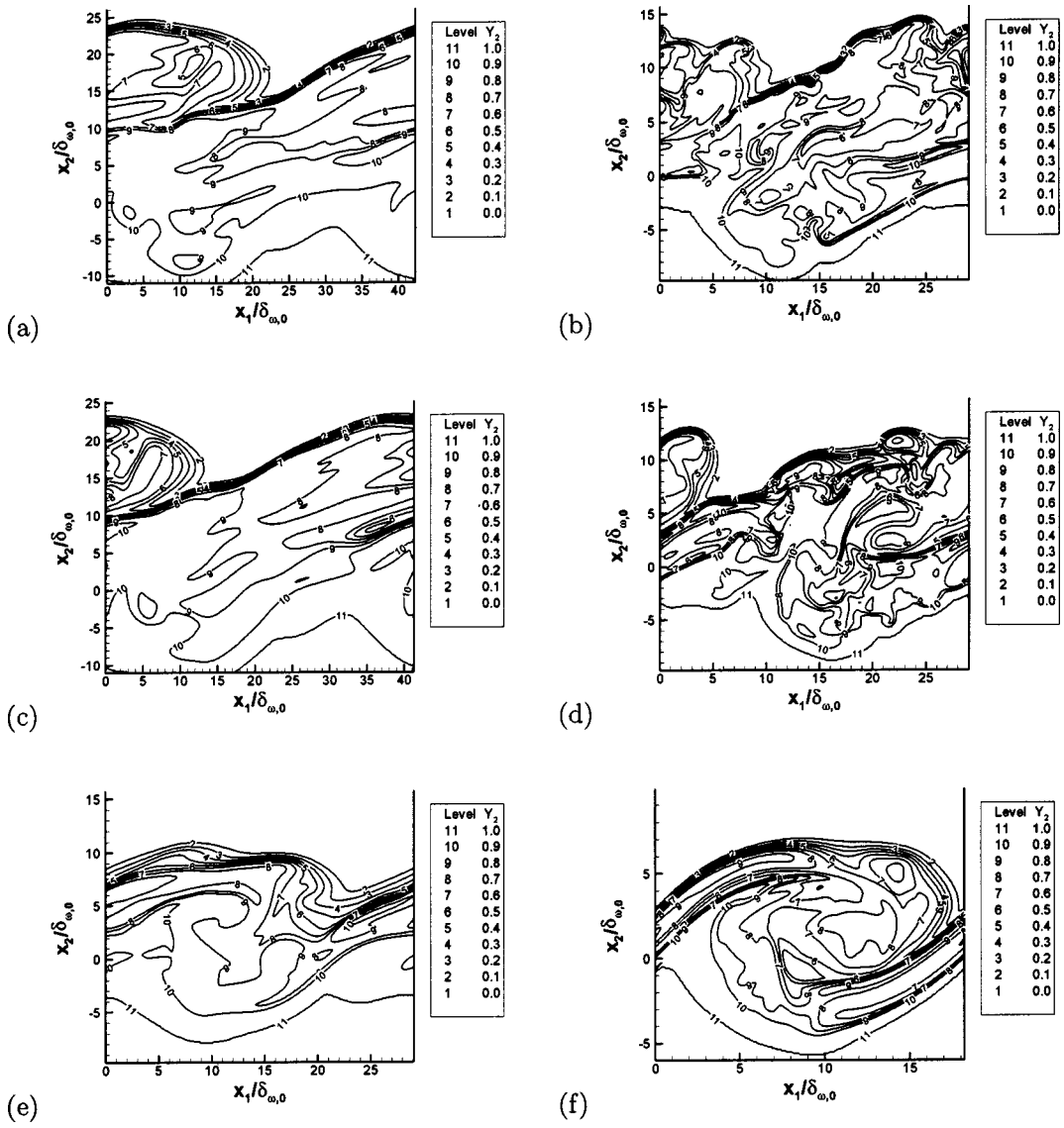

FIG. 6. Mass fraction for (a) OH500, (b) HN500, (c) OH550, (d) HN600, (e) OH750, and (f) HN800: In the braid plane ($x_3 = L_3/16$).

mate vortex. As discussed elsewhere,[10] the HN layers display substantial inhomogeneity due to the mixture nonideality and real gas behavior, with Z varying from 0.5 to 1 and α_D ranging from 0.55 to 1 for all HN layers; in contrast, the OH layers exhibit less inhomogeneity due to the high solubility of O_2 and H_2 and are close to perfect gases, ideal mixtures with both Z and α_D being close to unity.[11] Consistent with the discussion of the HDGM regions, the HN layers have about a factor of 2 larger $|\zeta|$ than their OH counterpart and the OH layers also have more localized high $|\zeta|$ regions, mostly confined to the lighter fluid side. The wider distribution of high $|\zeta|$ regions in the HN layers indicates more effective global mixing, as fluid regions with different composition are being brought into proximity; this information is consistent with the evolution of $\delta_p/\delta_{p,0}$ illustrated in Fig. 3(b). On the other hand, the larger $|\zeta|$ indicates less effective local mixing (through diffusion), due to the stronger mixture nonideality. Basically, the $C_7H_{16}-N_2$ system being far from mixture ideality and comparatively much less soluble, tends to maintain strong gradients in the mixing region; this result was also found for C_7H_{16} drops in N_2.[3] In contrast, the inherent mixing ability of the O_2-H_2 system (both solubility and mixture ideality) smears the mass fraction gradients.[30]

These different mixing characteristics of the O_2-H_2 and $C_7H_{16}-N_2$ systems have a significant impact on the flow through their effect on the dissipation.

C. Irreversible entropy production (dissipation)

Okong'o and Bellan[39] have shown that if g denotes the rate of irreversible entropy production for a single-phase binary-species flow devoid of sources or sinks, then

$$g = g_{\text{visc}} + g_{\text{temp}} + g_{\text{mass}}, \tag{18}$$

where

$$g_{\text{visc}} = \frac{\mu}{T} 2\left(S_{ij} - \frac{1}{3} S_{kk}\delta_{ij} \right)^2, \quad g_{\text{temp}} = \frac{\kappa}{T^2}\frac{\partial T}{\partial x_i}\frac{\partial T}{\partial x_i},$$

$$g_{\text{mass}} = \frac{1}{Y_1 Y_2 \rho D}\frac{R_u m}{m_1 m_2} j_{2i} j_{2i}. \tag{19}$$

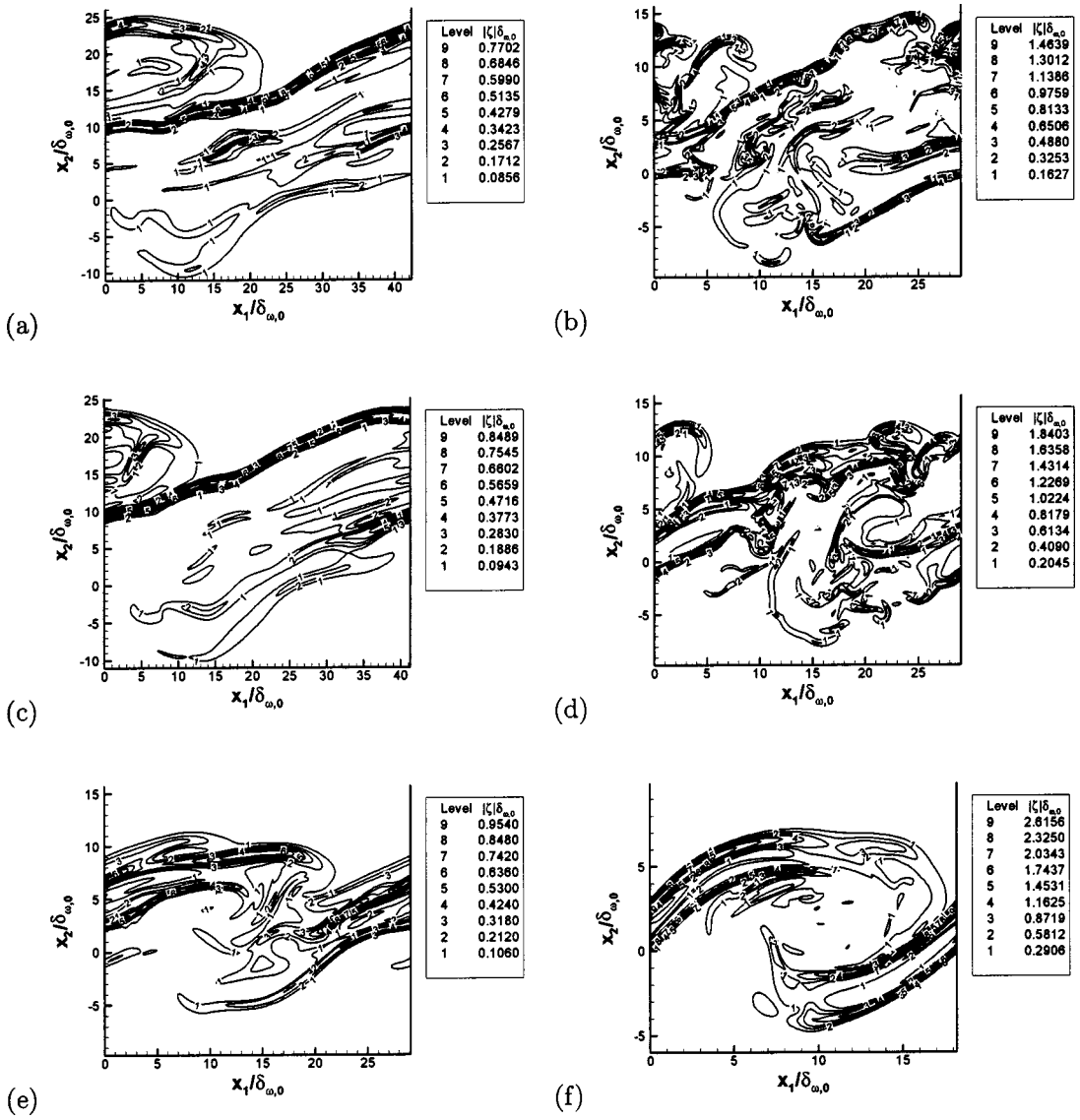

FIG. 7. Mass fraction gradient magnitude for (a) OH500, (b) HN500, (c) OH550, (d) HN600, (e) OH750, and (f) HN800: In the braid plane ($x_3 = L_3/16$).

Illustrated in Fig. 8 is g for the layers listed in Table IV, in the braid planes at the respective transitional times. All layers display localized regions of high dissipation. Comparing HN600 [Fig. 8(d)] and OH750 [Fig. 8(e)], which have a similar magnitude of $\mathrm{Re}_{m,tr}$ and are excited with the same $\lambda_1/\delta_{\omega,0}$ and $F_{3\mathrm{D}}$ (see Table IV), the magnitude of g is larger for the OH750 simulation. The regions of dissipation are also much more wide spread over the domain for the OH750 than for the HN600 layer. This larger activity in the dissipation for the OH750 layer is evidently responsible for its lower turbulence levels. Examination of the g plots for all layers shows that at same initial conditions, g augments with increasing Re_0 (HN500 versus HN600) or with combined decreasing $\lambda_1/\delta_{\omega,0}$ and increasing Re_0 (HN500 vs HN800, OH550 vs OH750).

As previously discussed,[10,11] independent of the species system, the regions of highest g magnitude are located within the HDGM regions; this can be clearly seen by comparing Figs. 5 and 8. However, whereas the highest g magnitude regions are observed in the lower stream for the OH layers, the HN layers exhibit the highest g magnitude regions in the upper stream. Comparison of Figs. 7 and 8 also reveals a strong visual correlation between high g and high $|\zeta|$ in that the upper stream high g regions correspond to high $|\zeta|$, and this feature is independent of the species system. However, subtle differences between the two species systems exist: For HN layers the lower stream high g regions comprise only a small portion of the high $|\zeta|$ regions, just as they do for the HDGM, whereas for the OH layers the lower stream g regions do not correlate with high $|\zeta|$ regions.

Therefore, the emerging picture, from Figs. 4–8 together with movies of the $|\nabla\rho|$ evolution, is of different dissipation mechanisms for OH than HN layers. For the HN layers, the largest dissipation occurs in the upper stream which has lighter fluid; these locations are within HDGM regions originating from fluid mixing rather than the original density stratification and therefore have high $|\zeta|$ but relatively low $|\nabla\rho|$; therefore, this mechanism can be partially attributed to the mixture nonideality, which is a thermodynamic effect. Although this mechanism is also active in the OH layers, it is

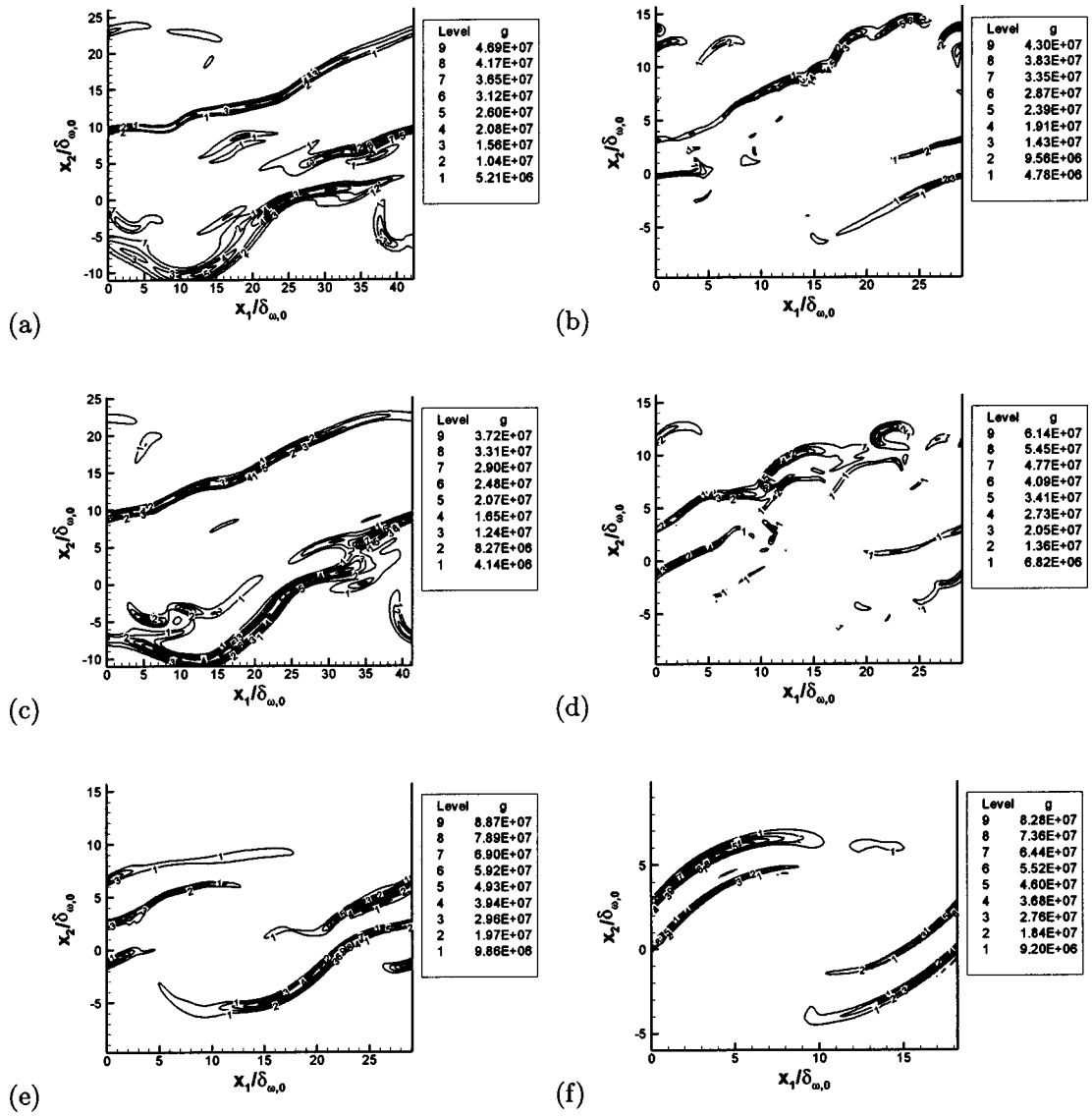

FIG. 8. Dissipation (in J/m^{3}K) for (a) OH500, (b) HN500, (c) OH550, (d) HN600, (e) OH750, and (f) HN800: In the braid plane ($x_3 = L_3/16$).

no longer the dominant one. Because the O_2-H_2 mixture is very nearly ideal, the major contribution to the dissipation is there from the lower layer regions located in the heavier fluid which originate from the distortion of the initial density stratification boundary and have high $|\nabla\rho|$ but low $|\zeta|$; therefore, this mechanism is dynamic in origin.

The correlation between HDGM, high $|\zeta|$ and high g regions is further studied by calculating the terms in Eqs. (18) and (19). The contributions to g for all layers are displayed in Fig. 9 in terms of homogeneous (x_1, x_3)-plane averages. For all layers, contributions from g_{mass} dominate those from g_{visc} and g_{temp}, although the viscous dissipation plays a much smaller role for $C_7H_{16}-N_2$ than for O_2-H_2 [Fig. 9(a)]. The dominance of g_{mass} over the other contributions means that it controls the behavior of g; then ζ and g will be directly related since, $g_{\text{mass}} \propto \mathbf{j}_2 \cdot \mathbf{j}_2$ [Eq. (19)], and $\mathbf{j}_2 \propto \zeta$ [Eqs. (7) and (9)]. For OH layers, the ∇p and ∇T contributions to $\mathbf{j}_2$ are negligible; the same is true for HN layers, except near the N_2 stream, where the ∇T contribution rivals the ∇Y_2 contribution. Furthermore, the relation between ζ and g will be modulated by the other factors multiplying the ζ term in $\mathbf{j}_2$, namely ρ and α_D. Examining the g_{mass} average plots [Fig. 9(c)] leads to similar conclusions as previously reached based on the g contour plots (Fig. 8): The largest peaks in g_{mass} are located for the OH layers on the O_2 side of the layer, corresponding to the HDGM regions, and with comparable peaks on the H_2 side, corresponding to large gradients in the mass fractions. For the HN layers, the largest peaks occur on the N_2 side, where the mass fraction gradients are large.

The impact of ζ on the layer characteristics through the dissipation motivates a more detailed examination of the processes leading to creation and/or distortion of mass fraction fronts.

D. Area production

For a fluid front oriented perpendicular to ζ and in a coordinate system moving with the relative velocity between the front and the flow, the stretch of the front is[18]

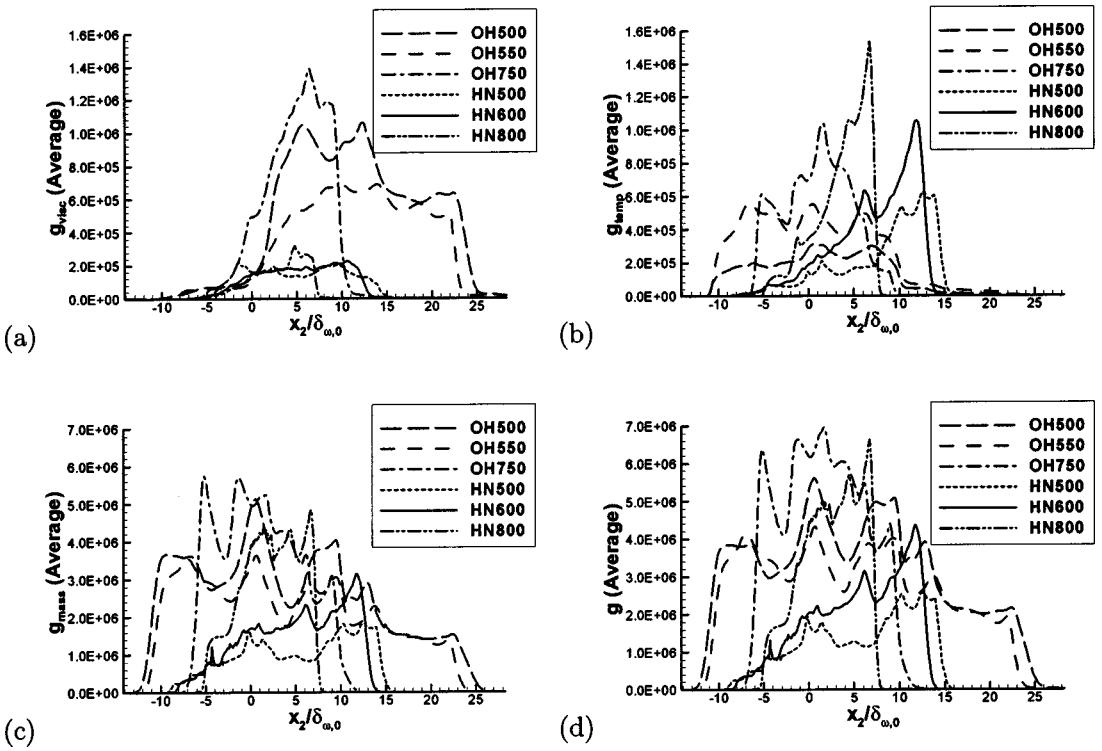

FIG. 9. Contributions to the dissipation (in J/m^{3}K) for all layers in Table IV: (a) Viscous, (b) temperature, (c) mass flux, and (d) total; averages in homogeneous planes.

$$\frac{1}{A}\frac{dA}{dt} = -\frac{(\zeta_i\zeta_j S_{ij})}{(\zeta_k\zeta_k)} + S_{kk}, \tag{20}$$

where A is the area of the front and the normal to the front is $n_i = -\zeta_i/\sqrt{\zeta_k\zeta_k}$. The term $(\zeta_i\zeta_j S_{ij})/(\zeta_k\zeta_k) = \zeta^T\mathbf{S}\zeta/|\zeta|^2$ represents the normal strain in the ζ-direction, in which $(-\zeta_i\zeta_j S_{ij})$ contains the interaction of $\mathbf{S}$ and ζ, while S_{kk} represents compressibility effects; thus both strain and diffusion processes (through ζ) affect area changes. We first examine the local activity of $(1/A)(dA/dt)$, evaluated from Eq. (20), by means of contour plots, and its homogeneous-plane average activity, after which we derive evolution equations for the terms on the right-hand side of Eq. (20) and assess their budgets.

1. Local and average activity in area production

Depicted in Fig. 10 are the transitional-state braid-plane contours of $(1/A)(dA/dt)$, as well as other terms appearing in Eq. (20), for the HN800 layer (corresponding plots for the other layers, not shown, yield similar conclusions). At the transitional states, much of the area-production activity is spatially concentrated at the edge of the coherent vortices, with substantial contribution from the interior of the mixing layer; thus, both large and small scales contribute to $(1/A)\times(dA/dt)$, which exhibits both positive and negative local regions. The $(1/A)(dA/dt)$ range for the OH layers is less than one-half that of the HN layers (not shown). Figure 10 shows that $(1/A)(dA/dt)$ correlates visually with $\zeta^T\mathbf{S}\zeta/|\zeta|^2$ and furthermore that they are close in magnitude; the correlation between $(1/A)(dA/dt)$ and S_{ii} is moderate. Since the range of S_{ii} values is only a factor of two smaller than that of $(-\zeta^T\mathbf{S}\zeta)/|\zeta|^2$, compressibility effects are seen to be locally important. Noteworthy, $(-\zeta^T\mathbf{S}\zeta)$ and $|\zeta|^2$ are very concentrated in ''wisps'' located within the HDGM regions; however, not all HDGM regions exhibit high $(-\zeta_i\zeta_j S_{ij})$ activity. Although, $S_{ij}S_{ij}$ shows only moderate visual correlation with $(1/A)(dA/dt)$, the most active $(-\zeta_i\zeta_j S_{ij})$ regions occur where high $S_{ij}S_{ij}$ and high $|\zeta|^2$ regions overlap, which leads to the correspondence between high $|\zeta|$ regions ($|\zeta|\delta_{\omega,0}>1$ in Fig. 7) and high $(-\zeta_i\zeta_j S_{ij})$ regions; this correspondence is though limited to the preponderant high magnitude positive $(-\zeta_i\zeta_j S_{ij})$ locations where there is gradient amplification by compressive straining.

The $(1/A)(dA/dt)$ evolution is presented in Fig. 11, in terms of homogenous-plane averages, at three physically meaningful times, the first and second pairing times, as well as the transition time. For the OH layers, $(1/A)(dA/dt)$ is overwhelmingly positive on average at the times analyzed. For these layers, at early times, there is a peak in $(1/A)\times(dA/dt)$ in the upper stream; this peak moves further into the upper stream while decreasing slightly in magnitude at later times. In contrast, for HN layers, at the first pairing time there is a peak of negative average $(1/A)(dA/dt)$ in the lower stream; then at later times, the $(1/A)(dA/dt)$ average is positive as was observed for OH layers. For the HN layers, the peak average $(1/A)(dA/dt)$ retains its magnitude at the second pairing and transition times, and moves only slightly further towards the upper stream. For all layers at the times in Fig. 11, on average, the dominant contribution to $(1/A)\times(dA/dt)$ is from the $(-\zeta_i\zeta_j S_{ij})/(\zeta_k\zeta_k)$ term, and $(-\zeta_i\zeta_j S_{ij})$ is positive on average. Therefore, the sign of the average $(1/A)(dA/dt)$, which may be negative, is due to the

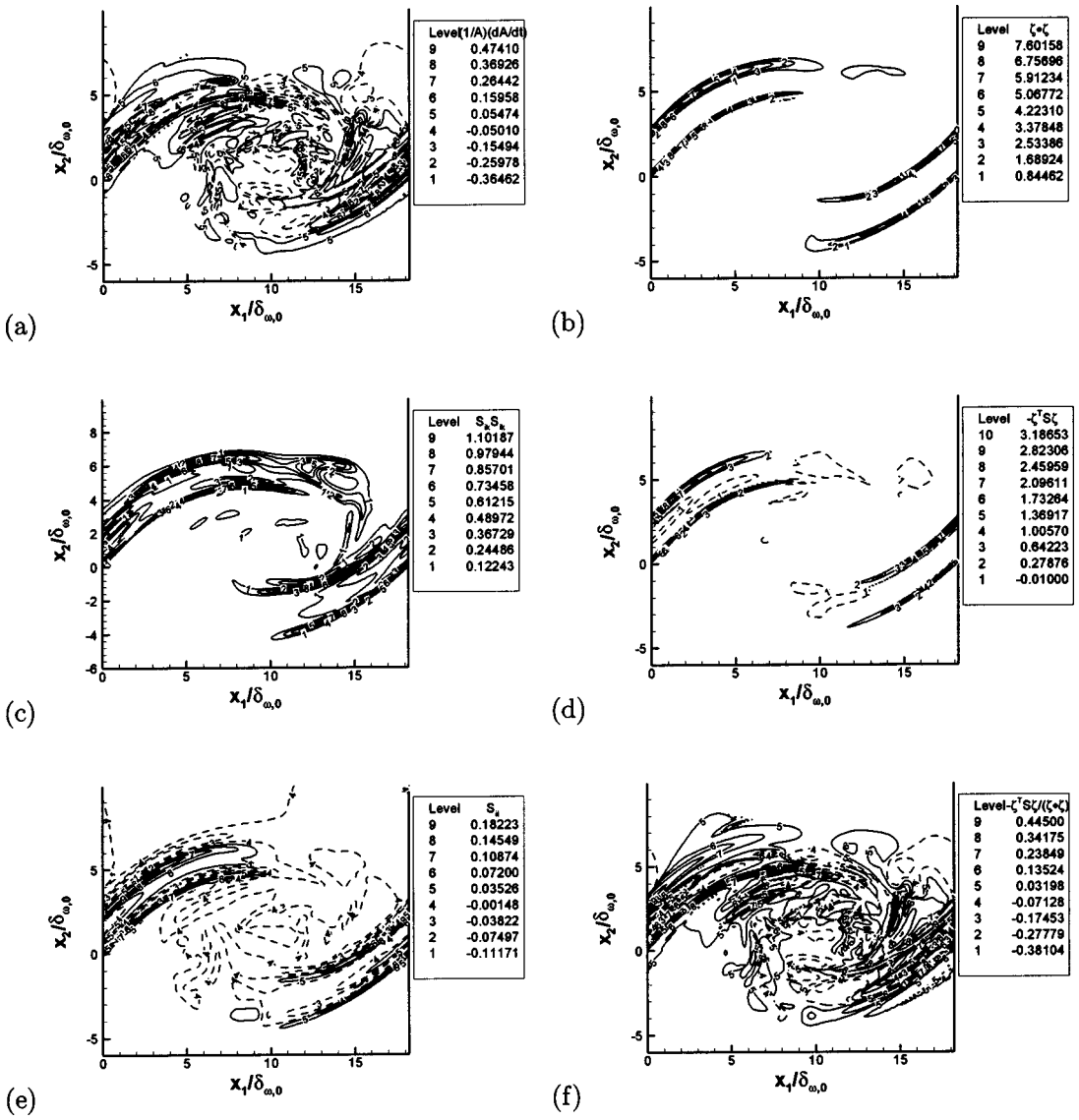

FIG. 10. $(1/A)(dA/dt)$ terms for the HN800 layer transitional state, (a) $(1/A)(dA/dt)(\delta_{\omega,0}/\Delta U_0)$, (b) $(\zeta_k\zeta_k)(\delta^2_{\omega,0})$, (c) $S_{ij}S_{ij}(\delta_{\omega,0}/\Delta U_0)^2$, (d) $-\zeta_i\zeta_jS_{ij}(\delta^3_{\omega,0}/\Delta U_0)$, (e) $S_{ii}(\delta_{\omega,0}/\Delta U_0)$ (f) $-\zeta_i\zeta_jS_{ij}/(\zeta_k\zeta_k)(\delta_{\omega,0}/\Delta U_0)$: In the braid plane ($x_3=L_3/16$). Dashed lines denote negative values.

biasing of $(-\zeta_i\zeta_jS_{ij})$ introduced when it is divided by $(\zeta_k\zeta_k)$. The division by $(\zeta_k\zeta_k)$ tends to reduce the magnitude of highly positive $(-\zeta_i\zeta_jS_{ij})$ while increasing the magnitude of slightly negative $(-\zeta_i\zeta_jS_{ij})$ (see Fig. 10), leading to possibly negative average $(1/A)(dA/dt)$ depending on the specific values of $(-\zeta_i\zeta_jS_{ij})$ and $(\zeta_k\zeta_k)$.

To compare area creation among layers, depicted in Fig. 12 are the homogeneous-plane averages and RMS of $(1/A)\times(dA/dt)$ for all layers at transition. The $(1/A)(dA/dt)$ average is overwhelmingly positive, with most area creation occurring inside the layers and on the lighter fluid side. Both the average and the RMS of $C_7H_{16}-N_2$ layers is about a factor of two larger than that of their O_2-H_2 counterpart, indicating that fluid disintegration is more effective and that fluctuations in the domain are much larger for the $C_7H_{16}-N_2$ layers. This finding regarding the magnitude of $(1/A)\times(dA/dt)$ averages for the two layer types is attributed to the smaller initial density stratification, $|\nabla\rho|\delta_{\omega,0}/\Delta\rho_0$, and the larger $(1/A)(dA/dt)$ RMS is conjectured to result from the complex interaction between the strength of the HDGM regions as measured by the value of $|\nabla\rho|\delta_{\omega,0}/\Delta\rho_0$ and the extent of their distribution in the domain. Essentially, in the O_2-H_2 layers there is globally less area production, but the area is created in a more spatially homogeneous manner than in their $C_7H_{16}-N_2$ counterpart. Also, area production seems uncorrelated with the magnitude of Re_m (see Table IV). Noteworthy, layers perturbed with a smaller $\lambda_1/\delta_{\omega,0}$ and having a larger Re_0 create more area on a cross-stream local basis, independent of the species system; this finding represents a first step towards area production control in turbulent supercritical fluids.

2. Evolution equations for terms determining area production

To further examine the area production, evolution equations are derived and further analyzed for each of the $(1/A)\times(dA/dt)$ terms. These equations

$$\frac{DS_{ii}}{Dt} = -S_{ik}S_{ik} + \frac{1}{2}\omega_i\omega_i - \frac{\partial}{\partial x_i}\left(\frac{1}{\rho}\frac{\partial p}{\partial x_i}\right) + \frac{\partial}{\partial x_i}\left(\frac{1}{\rho}\frac{\partial \tau_{ik}}{\partial x_k}\right), \tag{21}$$

$$\frac{1}{2}\frac{D(\zeta_i\zeta_i)}{Dt} = -\zeta_i\zeta_j S_{ij} - \zeta_i\frac{\partial}{\partial x_i}\left(\frac{1}{\rho}\frac{\partial j_{2k}}{\partial x_k}\right), \tag{22}$$

$$\begin{aligned}\frac{D}{Dt}(-\zeta_i\zeta_j S_{ij}) = {} & |\mathbf{D}^T\zeta|^2 + 2|\mathbf{S}\zeta|^2 - \frac{1}{2}|\omega\times\zeta|^2 \\ & + \zeta_i\zeta_j\frac{\partial}{\partial x_j}\left(\frac{1}{\rho}\frac{\partial p}{\partial x_i}\right) + 2\zeta_i S_{ij}\frac{\partial}{\partial x_j}\left(\frac{1}{\rho}\frac{\partial j_{2k}}{\partial x_k}\right) \\ & - \zeta_i\zeta_j\frac{\partial}{\partial x_j}\left(\frac{1}{\rho}\frac{\partial \tau_{ik}}{\partial x_k}\right),\end{aligned} \tag{23}$$

where $\mathbf{D}$ is the deformation tensor ($D_{ij}=\partial u_i/\partial x_j$), show that there are several source terms and fluxes that influence area production. A detailed discussion of the analysis of these equations using the DNS database is presented after some general considerations affecting Eqs. (21)–(23).

In Eq. (21), the first term describes self-interaction of strain, the second term contains the local vorticity effect, the third term represents the coupling of pressure and density variations, while the last term is the viscous diffusion. The quadratic form of the source terms in Eq. (21) is very suggestive: Vorticity enhances dilatation through rotational effects whereas strain decreases dilatation through stretching or compression; these observations are valid for a general flow.

In Eq. (22), $(-\zeta_i\zeta_j S_{ij})$ [which appears in Eq. (20)] is the source term of $(\zeta_k\zeta_k)$; $\zeta_k S_{ki}$ represents Y_2-gradient compression or stretching by strain. Recalling that Y_2 is not a passive scalar and that Y_2 is related to p by the EOS, ζ will affect the strain rate through ∇p which appears in Eq. (21).

On the right-hand side of Eq. (23), the first term represents the deformation (or convection) of ζ, the second term its compression or stretching by strain, and the third term is its rotation. The fourth term in Eq. (23) reflects the coupling between the spatial variations in the pressure, density and mass fraction, the fifth term is due to species mass diffusion and the last term represents viscous effects. The form of Eq. (23) is very evocative: For any flow, deformation and strain always increase $(-\zeta_i\zeta_j S_{ij})$ whereas the lack of alignment of ζ and ω always decreases $(-\zeta_i\zeta_j S_{ij})$. The effect of deformation and strain in increasing $(-\zeta_i\zeta_j S_{ij})$ can be understood by realizing that if ζ is amplified by deformation or compressive straining, the increase in ζ will result in the increase of $|\mathbf{D}^T\zeta|^2$ or $|\mathbf{S}\zeta|^2$ whereas if ζ is reduced by stretching, $\mathbf{D}$ or $\mathbf{S}$ is increased, which in turn increases $|\mathbf{D}^T\zeta|^2$ or $|\mathbf{S}\zeta|^2$. For given magnitudes of ζ and ω, the largest value of $|\omega\times\zeta|^2$, that is the largest reduction in $(-\zeta_i\zeta_j S_{ij})$, is obtained when $\zeta\perp\omega$ which means that the front is parallel to ω, enabling a very efficient stirring of the fluid. Noteworthy, because Eq. (22) shows that any effect increasing (decreasing) $(-\zeta_i\zeta_j S_{ij})$ also increases (decreases) $\zeta_k\zeta_k$, and since according to Eq. (20) it is the ratio $(-\zeta_i\zeta_j S_{ij})/(\zeta_k\zeta_k)$ that affects $(1/A)(dA/dt)$, no ultimate conclusion can be made regarding the influence of these effects on $(1/A)(dA/dt)$. Further insight into the phenomena governing the source terms of Eq. (23) can be obtained by rewriting

$$\begin{aligned}&|\mathbf{D}^T\zeta|^2 + 2|\mathbf{S}\zeta|^2 - \tfrac{1}{2}|\omega\times\zeta|^2 \\ &\quad = 3|\mathbf{S}\zeta|^2 - \tfrac{1}{4}|\omega\times\zeta|^2 - (\mathbf{S}\zeta)\cdot(\omega\times\zeta),\end{aligned} \tag{24}$$

because additional to the quadratic strain and rotational effects appearing in the right hand side of Eq. (24), the last term highlights the important effect of lack of isotropy of $\mathbf{S}$. Indeed, because $(\mathbf{S}\zeta)\cdot(\omega\times\zeta)=\omega\cdot[\zeta\times(\mathbf{S}\zeta)]=[(\mathbf{S}\zeta)\times\omega]\cdot\zeta$, it is clear that if $\mathbf{S}$ is isotropic, or if ω is parallel to either ζ or $(\mathbf{S}\zeta)$, or more generally to $\zeta\times(\mathbf{S}\zeta)$, this term would be null.

Thus, for any flow, vorticity increases S_{ii} but decreases $(-\zeta_i\zeta_j S_{ij})$, while strain has the opposite effect. In turn, $(-\zeta_i\zeta_j S_{ij})$ affects $\zeta_k\zeta_k$; although the sign of $(-\zeta_i\zeta_j S_{ij})$ cannot be determined in advance, if positive (negative) it increases (decreases) $\zeta_k\zeta_k$. Equations (21)–(23) do not reveal any information regarding the sign of $(-\zeta_i\zeta_j S_{ij})$ nor of the flux terms, which can only be ascertained when considering specific flows.

3. Analysis of budgets of S_{ii}, $\zeta_i\zeta_i$ and $(-\zeta_i\zeta_j S_{ij})$ at the transitional states

As a means of gaining insight into the specific physical mechanisms affecting area production in the present flows, we analyzed the budgets of the terms appearing in $(1/A)\times(dA/dt)$, so as to understand the observed differences between OH and HN layers at the transitional states (Fig. 12). Due to the use of a finite difference scheme in obtaining the DNS database, only a finite number of derivatives can be accurately computed on the grid. Higher order derivatives are less accurate, as they require repeated application of the first-derivative operator, and thereby have wider stencils. This problem is exacerbated for the present flow fields, particularly for HN layers, due to the narrowness of the regions of high $|\nabla\rho|$, $|\zeta|$ and $S_{ij}S_{ij}$. The problem was most noticeable on HN layers for terms involving $(\nabla\cdot\mathbf{j}_2)/|\zeta|^2$ (in the $(1/A)\times(dA/dt)$ evolution equation) and $\nabla p\cdot\nabla\rho$, and on all layers for terms involving $\nabla\rho(\nabla\cdot\mathbf{j}_2)$; such terms appear in the decomposition of the pressure-related fluxes in Eqs. (21) and (23):

$$\frac{\partial}{\partial x_i}\left(\frac{1}{\rho}\frac{\partial p}{\partial x_i}\right) = \frac{1}{\rho}\frac{\partial^2 p}{\partial x_i\partial x_i} + \frac{\partial}{\partial x_i}\left(\frac{1}{\rho}\right)\frac{\partial p}{\partial x_i}, \tag{25}$$

$$\zeta_i\zeta_j\frac{\partial}{\partial x_j}\left(\frac{1}{\rho}\frac{\partial p}{\partial x_i}\right) = \frac{1}{\rho}\zeta_i\zeta_j\frac{\partial^2 p}{\partial x_i\partial x_j} + \zeta_i\zeta_j\frac{\partial}{\partial x_j}\left(\frac{1}{\rho}\right)\frac{\partial p}{\partial x_i}. \tag{26}$$

For each of Eqs. (25) and (26), the first term in the right hand side involves $\partial^2 p/\partial x_i\partial x_j$, the Hessian of p. In the constant density flows of She *et al.*,[40] Ohkitani and Kishiba[41] and Nomura and Post,[42] the second term of Eq. (25) was null and the pressure Hessian could be considered as a nonlocal effect since in those flows it can only be expressed as an integral by solving a Poisson equation over the entire domain (see Oh-

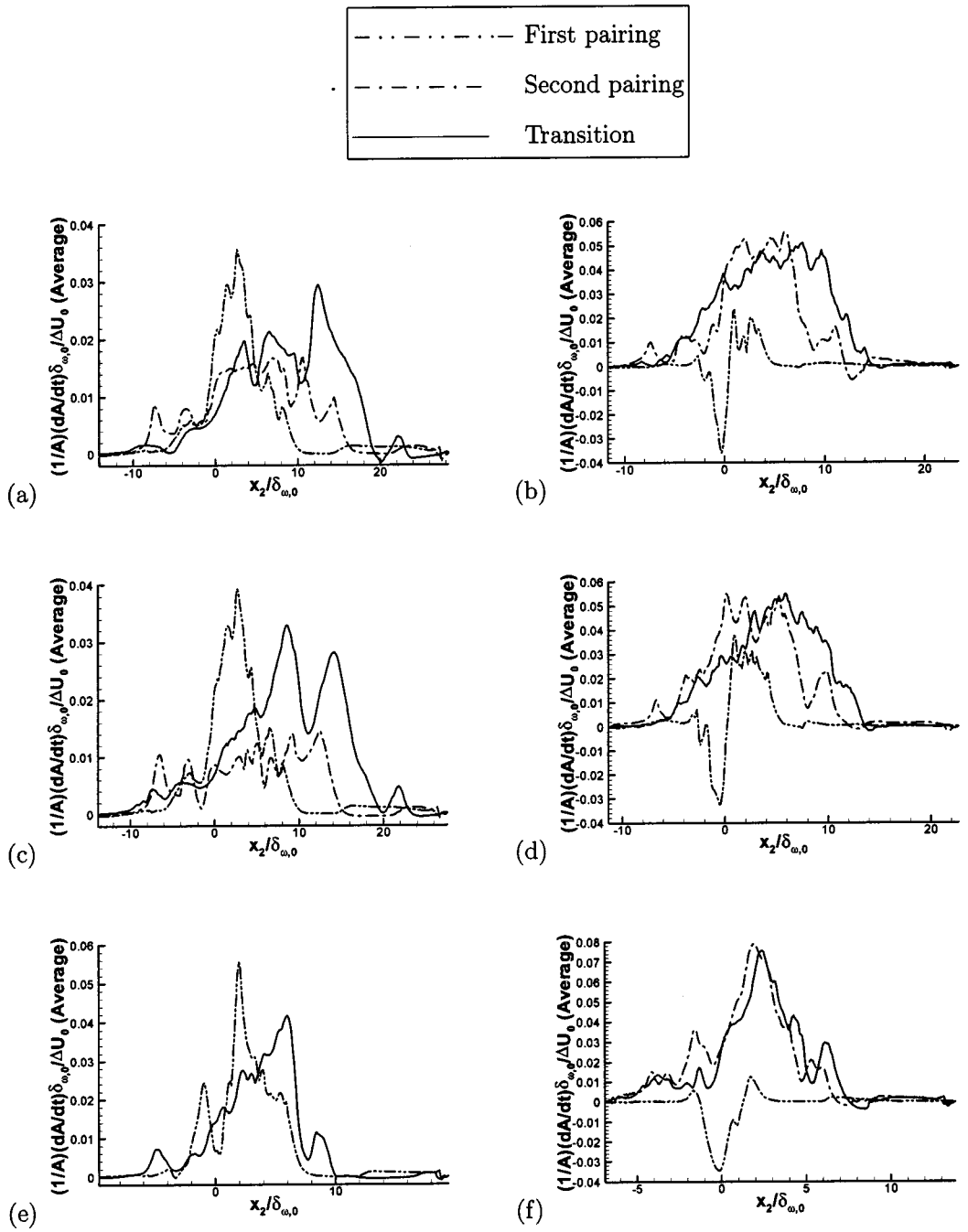

FIG. 11. $(1/A)(dA/dt)$ at various times for (a) OH500, (b) HN500, (c) OH550, (d) HN600, (e) OH750, and (f) HN800: Average in (x_1, x_3) planes. (Note: For OH750, second pairing time and transition time are the same.)

kitani and Kishiba[41]); the pressure is then a dynamic quantity that can be computed using only the velocity field. In contrast, for the present compressible flows, the pressure is a thermodynamic quantity computed from ρ, e, and Y_2 using the EOS and therefore the pressure Hessian does not have the same significance, representing now a local effect. Computations of the two terms on the right-hand sides of Eqs. (25) and (26), accurate only for OH layers, revealed that the first term dominates the second, although not as strongly in Eq. (26) as in Eq. (25), representing a modulating effect of ζ. These conclusions are not necessarily valid for HN layers, particularly in the HDGM regions. Due to the aforementioned numerical difficulties, we here restrict our analysis to Eqs. (21)–(23), for which we can reliably compare HN and OH layers. Although the value of the terms in Eqs. (21)–(23) is different at each of the times analyzed, their ordering is similar to that obtained at the transitional state.

a. Budget of S_{ii}. Figure 13 illustrates the homogeneous plane averages and RMS for the OH750 and HN600 layers, chosen for comparison because of similar Re_m; the discussion below is based on the examination of the equivalent plots for all layers. The flux terms in Eq. (21) are on average negligible for all layers with respect to the source terms. Since viscosity is associated with dissipation, but not directly with the structure of the flow, viscous effects are not expected to influence compressibility, as borne out by Fig. 13.

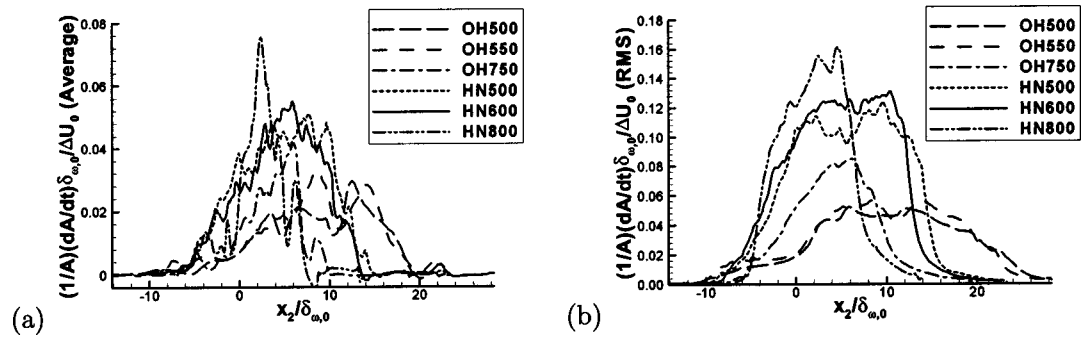

FIG. 12. $(1/A)(dA/dt)$ at the respective transitional states: (a) average and (b) RMS in (x_1,x_3) planes for all layers listed in Table IV.

While Eq. (21) showed that the strain effect would always be negative, counteracting the positive vorticity effect, Fig. 13 shows that these two terms are of comparable magnitude for the OH750 and HN600 layers, and indeed for all layers. Considering the RMS, whereas for the OH layers the source terms dominate, followed closely by $\nabla\cdot(\nabla p/\rho)$, in the HN layers, it is generally $\nabla\cdot(\nabla p/\rho)$ that tends to be the largest; this difference between the OH and HN systems is attributed to the stronger coupling between p and ρ for the latter system which manifests itself by considerable departures from a perfect gas and an ideal mixture. This coupling is in the magnitudes of ∇p and $\nabla(1/\rho)$ and not in their directions, as the probability density functions (PDFs) of $\cos(\nabla p,\nabla(1/\rho))$ in Fig. 14 show that all layers have similar alignments, with ∇p and $\nabla(1/\rho)$ being most likely counter-aligned or aligned.

b. Budget of $\zeta_i\zeta_i$. The evolution of $(\zeta_i\zeta_i)/2$ [Eq. (22)] is the result of the source term $(-\zeta^T\mathbf{S}\zeta)$ and the flux term $\{-\zeta\cdot\nabla[(\nabla\cdot\mathbf{j}_2)/\rho]\}$; the planar averages of these terms are

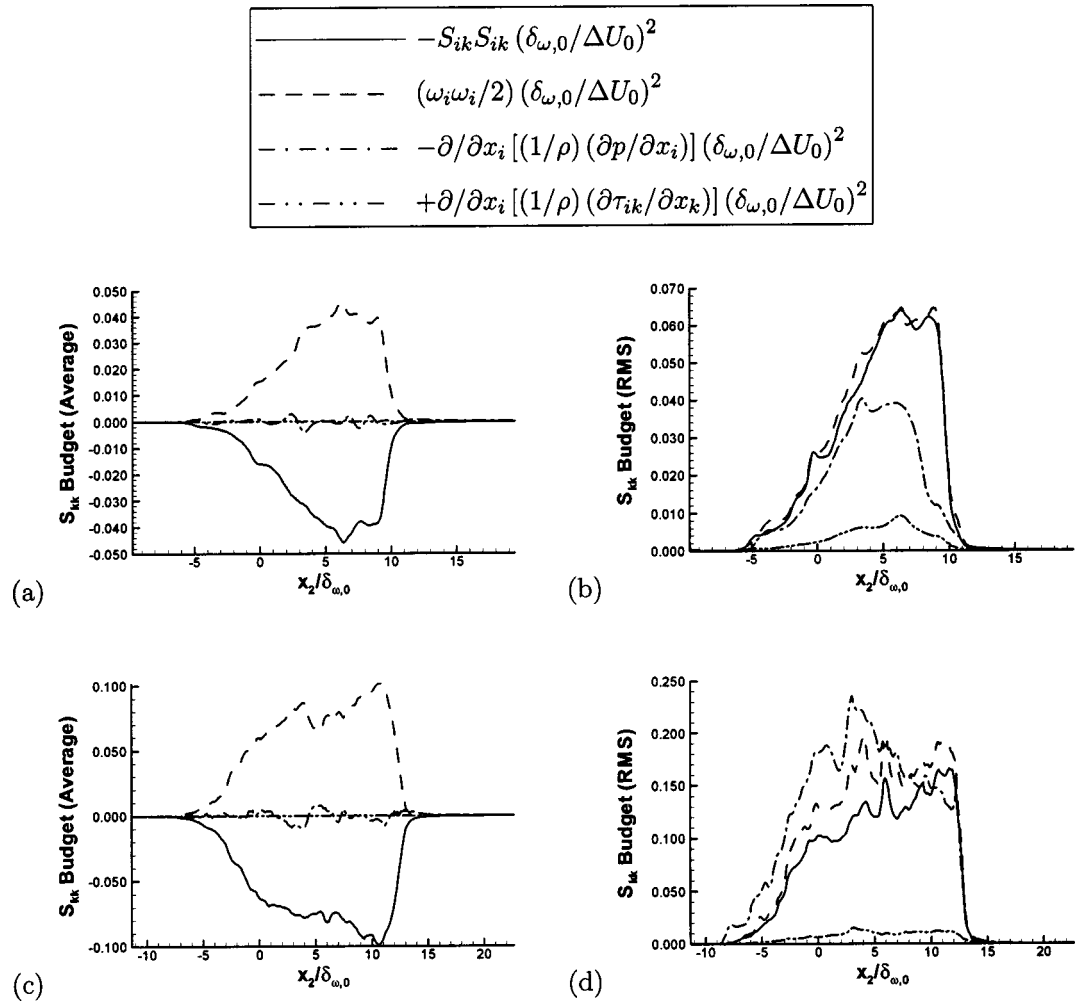

FIG. 13. Budget of DS_{kk}/Dt at the respective transitional states for (a) and (b) OH750 and (c) and (d) HN600: (a) and (c) averages and (b) and (d) RMS in (x_1,x_3) planes.

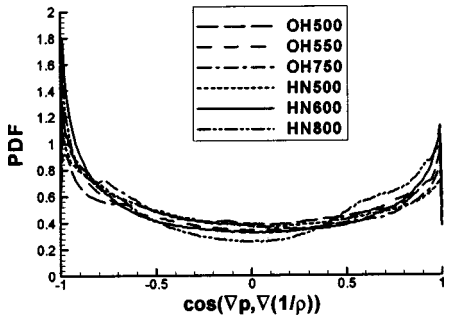

FIG. 14. Probability density functions of $\cos[\nabla p,\nabla(1/\rho)]$ at the respective transitional states for all layers listed in Table IV. For points within the layer $(0.005 \leqslant Y_2 \leqslant 0.995)$.

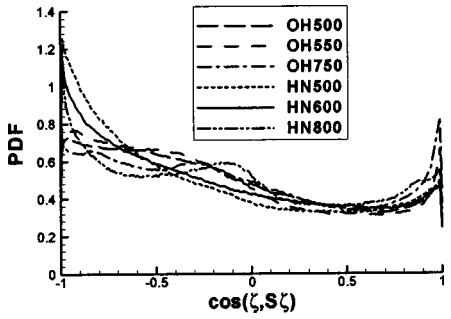

FIG. 16. Probability density function of $\cos(\zeta,\mathbf{S}\zeta)$ at the respective transitional states for all layers listed in Table IV. For points within the layer $(0.005 \leqslant Y_2 \leqslant 0.995)$.

shown in Fig. 15. The two terms are seen to counteract each other, being positive and negative, on average, while having similar magnitudes. The negative sign of the average $\{-\zeta \cdot \nabla[(\nabla \cdot \mathbf{j}_2)/\rho]\}$ is due to the counteracting effect of $\mathbf{j}_2$ on ζ: If ζ increases (decreases), so does $\mathbf{j}_2$, which hinders the ζ increase (decrease). The $(-\zeta_i\zeta_j S_{ij})$ plot in Fig. 15 shows that the HN800 layer is significantly more active than the other layers, with the least activity observed for the OH500 and OH550 layers, similar to the findings for $(1/A) \times (dA/dt)$. The location of the $(1/A)(dA/dt)$ peak for HN800 correlates to that of $(-\zeta_i\zeta_j S_{ij})$, although the curves have drastically different profiles. To further inquire into the sign of the $(-\zeta^T\mathbf{S}\zeta)$ values, we calculated the PDF of $\cos(\zeta,\mathbf{S}\zeta)$, illustrated in Fig. 16, which shows that anti-alignment and alignment are the most likely orientations, although the HN800 layer has a local minor peak in the PDF where ζ and $\mathbf{S}\zeta$ are nearly perpendicular. For all layers, $\cos(\zeta,\mathbf{S}\zeta)$ is more likely to be negative than positive, i.e., the angle between ζ and $\mathbf{S}\zeta$ is mostly between $\pi/2$ and $3\pi/2$; this explains why $(-\zeta_i\zeta_j S_{ij})$ is positive on average.

c. Budget of $(-\zeta_i\zeta_j S_{ij})$. To assess the relative importance of the terms in Eq. (23), depicted in Figs. 17 and 18 are the homogenous-plane averages and RMS, respectively, of the terms for all layers. Most of the activity occurs on the light fluid side of the layer, whether for the average or for the RMS. Compared to the $C_7H_{16}-N_2$ layers, the average and RMS are for O_2-H_2 layers one and two orders of magnitude smaller, respectively, indicating a more subdued activity. Consistent with the $(1/A)(dA/dt)$ results, the HN800 layer is the most active. On average (Fig. 17), the largest magnitude terms are $2|\mathbf{S}\zeta|^2$ and $\frac{1}{2}|\omega\times\zeta|^2$, followed by $|\mathbf{D}^T\zeta|^2$ and by $2\zeta\cdot\mathbf{S}\cdot\nabla[(\nabla\cdot\mathbf{j}_2)/\rho]$ which is mostly negative. The negative effect of the flux term can be traced to the fact that if ζ is amplified (attenuated) by compression (stretching) from strain, diffusion is promoted (hindered), counteracting the effect of ζ amplification (attenuation). Generally, on average the strain term balances the rotational term while the mass flux term counteracts the convective term; on average, each pair of terms has comparable magnitude and similar location of peaks. The next term in decreasing importance is $\zeta_i\zeta_j\partial/\partial x_j[(1/\rho)(\partial p/\partial x_i)]$ which is mostly negative, except near the edge of the layer on the light fluid side. Finally, the smallest term in the budget is that associated with the viscous stresses. This ordering of the viscous and ∇p terms is similar to that for the S_{ii} equation (Fig. 13). For the RMS (Fig. 18), the viscous term is always smallest, as was observed for the corresponding term in the S_{ii} equation (Fig. 13). For all layers, of the source terms, $2|\mathbf{S}\zeta|^2$ has the largest RMS values, followed by $\frac{1}{2}|\omega\times\zeta|^2$ and $|\mathbf{D}^T\zeta|^2$. Also for all layers, the flux term RMS is larger than that of $|\mathbf{D}^T\zeta|^2$; the flux term is also smaller than the strain and vorticity terms, except for some locations in the OH layers. In contrast to the RMS for OH layers, for HN layers the pressure term is dominant (except near the layer edges where it may be superseded by strain and vorticity effects) while for OH layers it is close in magnitude to the smallest, viscous, term and much smaller than the dominant strain term. The dominance of the pressure term in the RMS for HN layers is similar to that observed for the S_{ii} equation (Fig. 13), but seems to be enhanced in the $(-\zeta_i\zeta_j S_{ij})$ budget. Superimposing braid and between-the-

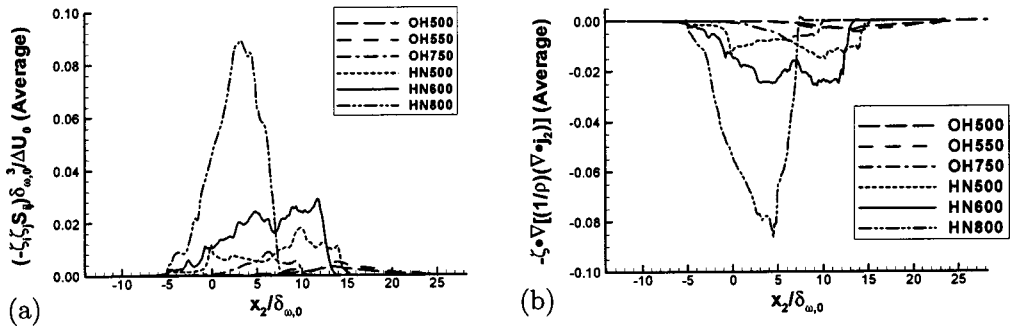

FIG. 15. Budget of $D(\zeta_k\zeta_k)/Dt$ at the respective transitional states (a) $(-\zeta_i\zeta_j S_{ij})$, (b) $-\zeta_i\partial/\partial x_i[(1/\rho)(\partial j_{2k}/\partial x_k)]$: Averages in (x_1,x_3) planes for all layers listed in Table IV.

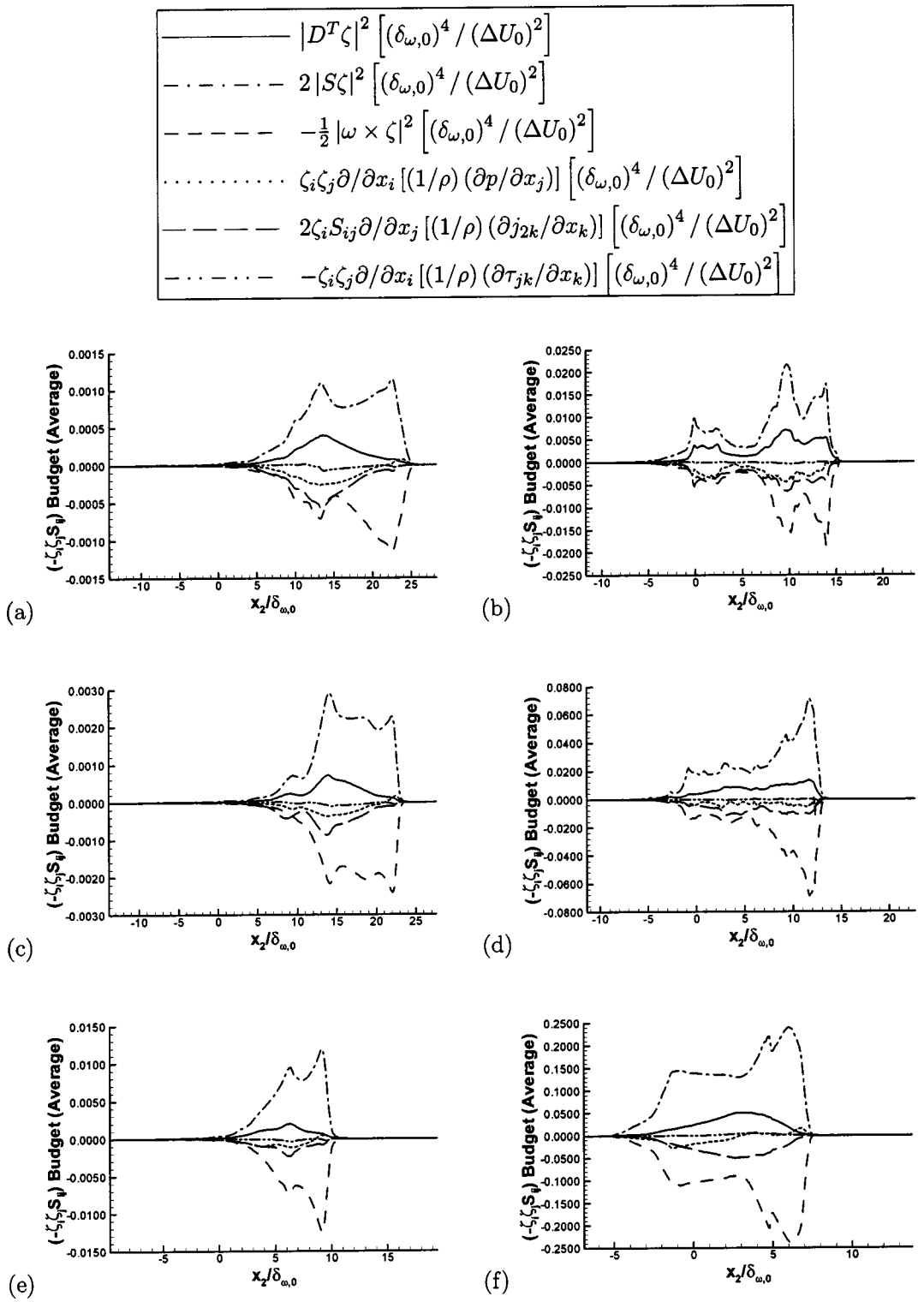

FIG. 17. Budget of $D(-\zeta_i\zeta_j S_{ij})/Dt$ at the respective transitional states for (a) OH500, (b) HN500, (c) OH550, (d) HN600, (e) OH750, and (f) HN800: averages in (x_1, x_3) planes.

braid contour plots of $|\nabla\rho|$, $|\nabla p|$ and $\zeta\zeta\nabla(\nabla p/\rho)$ led to the conclusion that whereas in the $C_7H_{16}-N_2$ layers the regions of $\zeta\zeta\nabla(\nabla p/\rho)$ activity coincided with the overlap of the significant $|\nabla p|$ with the HDGM regions, no such behavior existed for the O_2-H_2 layers. The PDFs of the cosines of the angles between ζ, ∇p and $\nabla(1/\rho)$, depicted in Figs. 14 and 19, show that for all layers, ζ and $\nabla(1/\rho)$ are overwhelmingly likely to be counter-aligned, while ζ and ∇p are most likely aligned or counter-aligned and ∇p and $\nabla(1/\rho)$ are most likely counter-aligned or aligned. Furthermore, the PDFs are similar for OH and HN layers, precluding the possibility that the large RMS values of $\zeta\zeta\nabla(\nabla p/\rho)$ for HN layers are due to their having stronger ζ, ∇p and $\nabla(1/\rho)$ alignments than do OH layers. Considering that for the (p,T) conditions of the

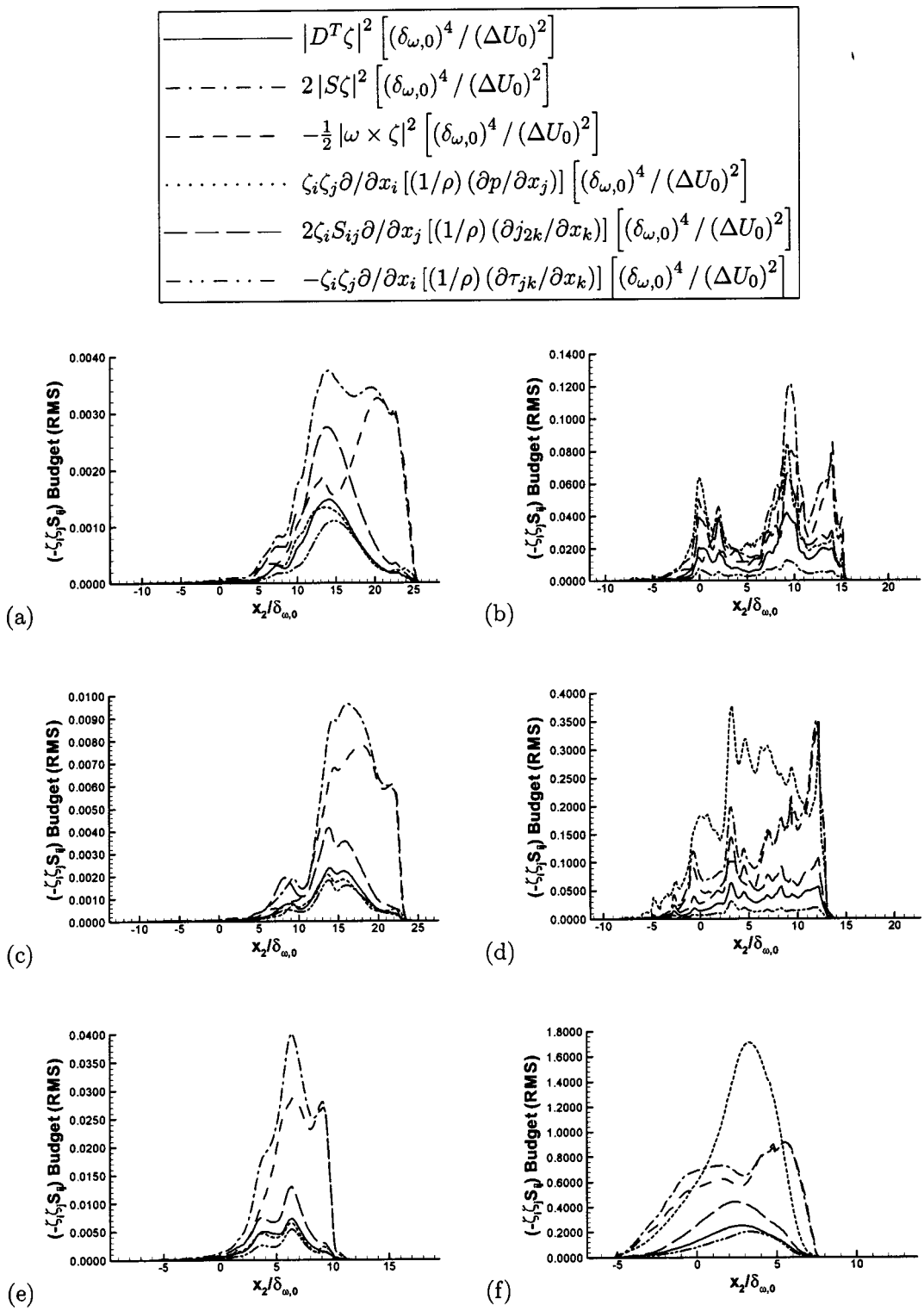

FIG. 18. Budget of $D(-\zeta_i\zeta_j S_{ij})/Dt$ at the respective transitional states for (a) OH500, (b) HN500, (c) OH550, (d) HN600, (e) OH750, and (f) HN800: RMS in (x_1, x_3) planes.

O_2-H_2 layers both fluids are quite close to perfect gases[11] compared to the $C_7H_{16}-N_2$ layers where strong departures from perfect gas behavior are exhibited,[9,10] the large contribution of $\zeta\zeta\nabla(\nabla p/\rho)$ to the $(-\zeta_i\zeta_j S_{ij})$ RMS is attributed to the strong p coupling with ρ through the real gas EOS.

Thus, for these specific OH and HN flows, viscous effects on S_{ii} evolution [Eq. (21)] and on $(-\zeta_i\zeta_j S_{ij})$ evolution [Eq. (23)] are on average negligible. Mass flux effects decrease both $(-\zeta_i\zeta_j S_{ij})$ and $(\zeta_k\zeta_k)$. In the $(\zeta_k\zeta_k)$ evolution [Eq. (22)], the mass flux effects balance $(-\zeta_i\zeta_j S_{ij})$, being on average of similar magnitude but negative, while $(-\zeta_i\zeta_j S_{ij})$ is on average positive. Mass flux effects are also significant in the $(-\zeta_i\zeta_j S_{ij})$ evolution, where they counteract the strain effect which always increases $(-\zeta_i\zeta_j S_{ij})$; on

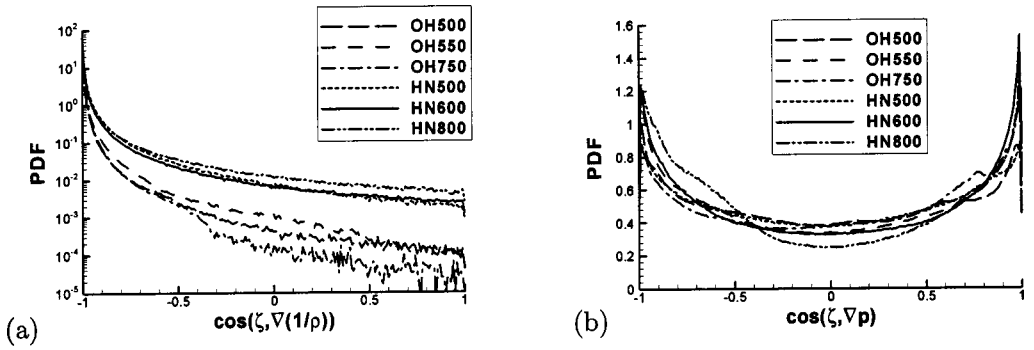

FIG. 19. Probability density functions of (a) $\cos(\zeta,\nabla(1/\rho))$ and (b) $\cos(\zeta,\nabla p)$ at the respective transitional states for all layers listed in Table IV. For points within the layer $(0.005 \leqslant Y_2 \leqslant 0.995)$.

average, these are the two largest magnitude terms. For the S_{ii} evolution, vorticity and strain effects, which have opposing signs, have on average similar magnitudes; the same is observed for vorticity and deformation effects in $(-\zeta_i\zeta_j S_{ij})$ evolution. While on average, pressure effects are small for all layers, the RMS reveals substantially more activity in HN layers than in OH layers. The RMS of the pressure term in both the S_{ii} and $(-\zeta_i\zeta_j S_{ij})$ equations exceeds only the viscous term for OH layers, while for HN layers, it tends to be the dominant term. Alignments of ζ, ∇p and $\nabla(1/\rho)$ were similar for all layers, therefore the greater activity for HN layers was attributed to stronger coupling between regions having large magnitudes of these terms, due to real gas behavior and mixture nonideality.

4. Vorticity–mass-fraction-gradient scalar product

Complementary to the strain-based analysis just presented is the inquiry into fluid-front area production through interaction of vorticity and mass fraction gradient.[15] Figure 20 shows the $(\omega\cdot\zeta)$ average and RMS, as well as the $|\omega|$ and $|\zeta|$ averages. The low average value of $(\omega\cdot\zeta)$ compared to that of its RMS, as well as to the values of $|\omega|$ and $|\zeta|$, suggests regions of significant positive and negative activity which globally cancel each other. Similar to the $(1/A)\times(dA/dt)$ results (Fig. 12), HN800 displays the most activity, while OH500 and OH550 display the least. Since $(\omega\cdot\zeta)$ displays features different from $|\omega|$ and $|\zeta|$, this motivated an

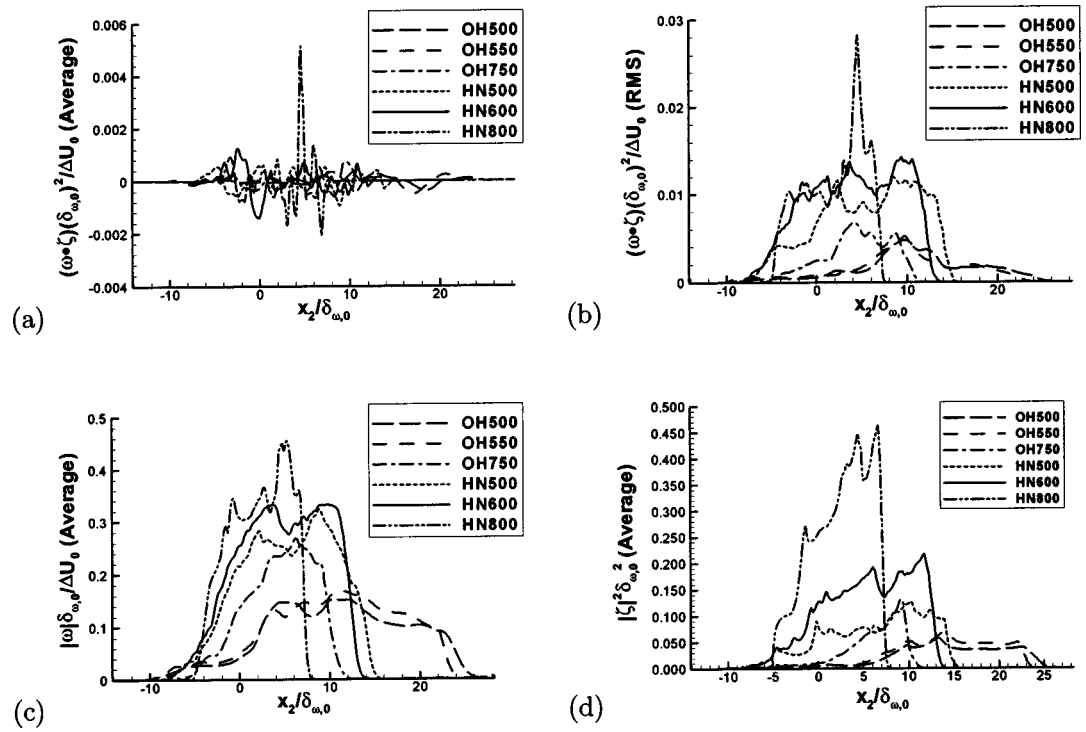

FIG. 20. $(\omega\cdot\zeta)$ at the respective transitional states: (a) Average $(\omega\cdot\zeta)$, (b) RMS $(\omega\cdot\zeta)$, (c) average $|\omega|$ and (d) average $|\zeta|$, in (x_1,x_3) planes for all layers listed in Table IV.

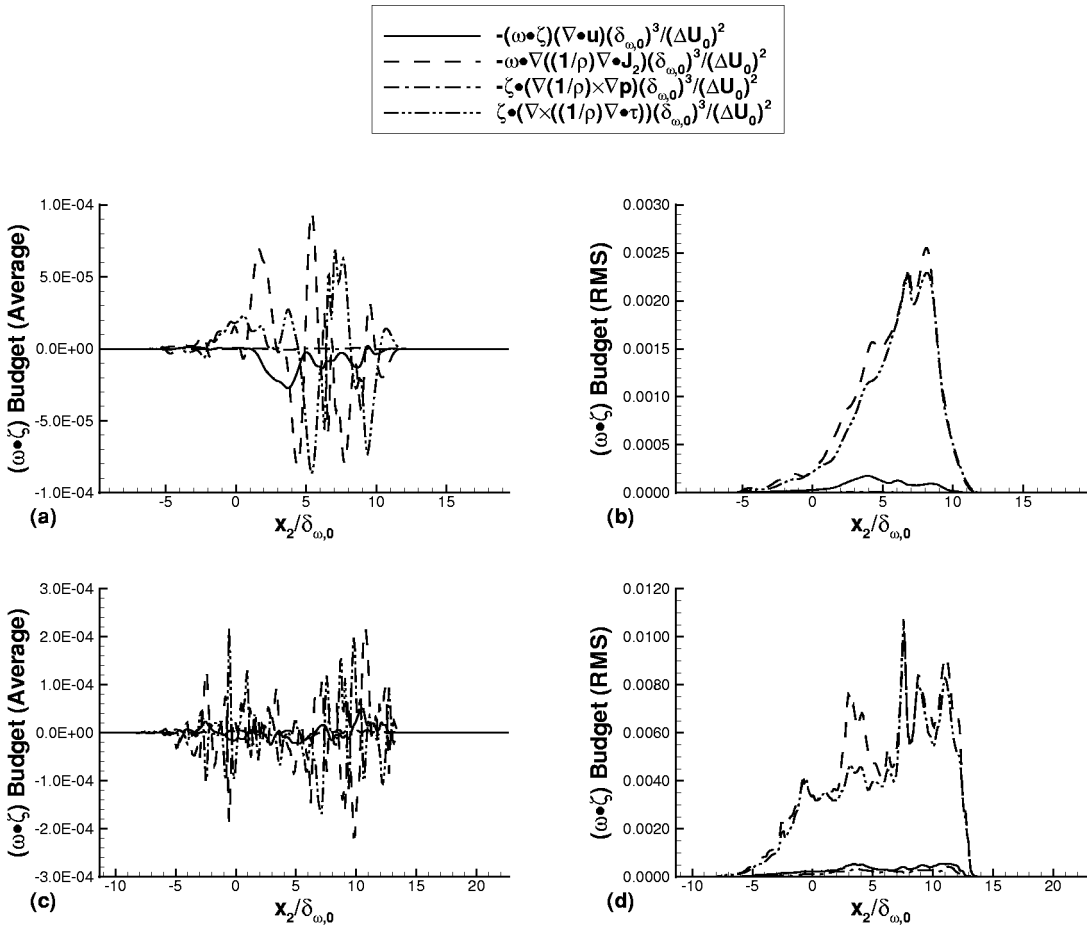

FIG. 21. Budget of $D/Dt(\omega\cdot\zeta)$ at the respective transitional states for (a) and (b) OH750 and (c) and (d) HN600: (a) and (c) averages and (b) and (d) RMS in (x_1,x_3) planes.

investigation of the ω to ζ alignment [whose effect also appears in Eq. (23)], which is presented in Sec. III D 5.

To inquire into the processes responsible for the evolution of $(\omega\cdot\zeta)$, an equation for it was derived from Eqs. (2) and (3), yielding

$$\frac{D}{Dt}(\omega\cdot\zeta)=-(\omega\cdot\zeta)(\nabla\cdot\mathbf{u})-\omega\cdot\left[\nabla\left(\frac{1}{\rho}\nabla\cdot\mathbf{j}_2\right)\right]-\zeta\cdot\left[\nabla\left(\frac{1}{\rho}\right)\times\nabla p\right]+\zeta\cdot\left[\nabla\times\left(\frac{1}{\rho}\nabla\cdot\bar{\bar{\tau}}\right)\right]. \quad (27)$$

In Eq. (27), the first term in the right hand side represents the effect of dilatation, the second term is due to species mass diffusion, the third term is due to the baroclinic contribution, and the last one represents the viscous effects. (The evolution of ω has previously been studied;[10,11] the divergence and baroclinic terms were found to be secondary, but significant, in magnitude.) Displayed in Fig. 21 are averages and RMS of the $D(\omega\cdot\zeta)/Dt$ budgets of the OH750 and HN600 layers; equivalent plots for the other layers (not shown) are similar. Locally in $x_2/\delta_{\omega,0}$, viscous and species mass flux effects dominate both the average and RMS, with dilatation and baroclinic-induced contributions being minimal and negligible, respectively. This means that locally in $x_2/\delta_{\omega,0}$, $(\omega\cdot\zeta)$ reflects the nonideality of the mixture through the species mass flux, in which the term $\propto\alpha_D$ is largest in Eq. (7).[10,11] However, if V is the volume of the entire domain, lengthy mathematics leads from Eq. (27) to

$$\int_V\frac{D}{Dt}(\omega\cdot\zeta)dV=-\int_V(\omega\cdot\zeta)(\nabla\cdot\mathbf{u})dV, \quad (28)$$

so that it is clear that the dilatation is volumetrically the sole feature influencing the variation of $(\omega\cdot\zeta)$ in the entire domain. A consequence of Eq. (28) is that if $dV/dt=0$ (as herein), then $\partial(\int_V(\omega\cdot\zeta)dV)/\partial t=0$, which makes this integral a time invariant for V.

Since orthogonality of ω and ζ implies $\omega\cdot\zeta=0$, the conceptual picture of Ruetsch and Ferziger[15] that orthogonality promotes area production can now be examined in light of Eq. (28); the following discussion assumes that, in this picture, only the relative orientations of ω and ζ change, not their magnitudes. From Eq. (20), locally we require $(\zeta_i\zeta_jS_{ij})/(\zeta_k\zeta_k)>\nabla\cdot\mathbf{u}$ in order to induce an increase in area. Equation (28) shows that, where $\nabla\cdot\mathbf{u}>0$, locally $(\omega\cdot\zeta)<0$ will increase itself, while $(\omega\cdot\zeta)>0$ will decrease itself; then dilatation acts similar to a "restoring force," always driving ω and ζ toward orthogonality, and consequently toward the greatest decrease in $(-\zeta_i\zeta_jS_{ij})$ according Eq. (23). From Eq. (20), if $\nabla\cdot\mathbf{u}>0$ and $(-\zeta_i\zeta_jS_{ij})>0$, $(1/A)(dA/dt)>0$ and

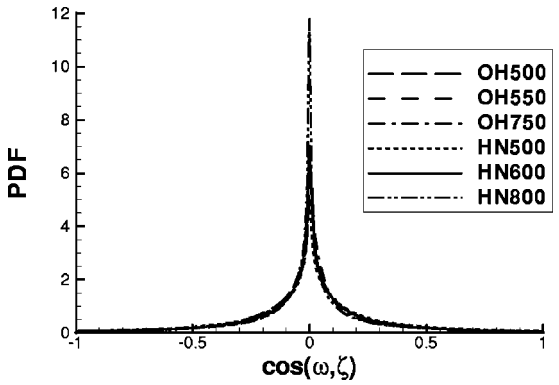

FIG. 22. Probability density function of $\cos(\omega,\zeta)$ at the respective transitional states for all layers listed in Table IV. For points within the layer $(0.005 \leqslant Y_2 \leqslant 0.995)$.

$(1/A)(dA/dt)$ may remain positive despite the decrease in $(-\zeta_i\zeta_j S_{ij})$ because, according to Eq. (22), $(-\zeta_i\zeta_j S_{ij})>0$ also increases $(\zeta_k\zeta_k)$. On the other hand, where $\nabla\cdot\mathbf{u}<0$, locally $(\omega\cdot\zeta)>0$ will increase itself, while $(\omega\cdot\zeta)<0$ will decrease itself; then dilatation acts as an instability, driving ω and ζ away from orthogonality; from Eq. (23), the interaction of ω and ζ always decreases $(-\zeta_i\zeta_j S_{ij})$ with the limiting case of no change in $(-\zeta_i\zeta_j S_{ij})$ when ω and ζ are parallel. From Eq. (20), if $\nabla\cdot\mathbf{u}<0$ and $(-\zeta_i\zeta_j S_{ij})<0$, $(1/A)\times(dA/dt)<0$; since $(-\zeta_i\zeta_j S_{ij})<0$ decreases $(\zeta_k\zeta_k)$ while $(-\zeta_i\zeta_j S_{ij})$ will decrease (or remain unchanged), area is destroyed. If $\nabla\cdot\mathbf{u}$ and $(-\zeta_i\zeta_j S_{ij})$ have opposite signs, $(1/A)\times(dA/dt)$ may be positive or negative depending on the magnitudes of the two terms, and if positive may remain so despite the decrease in $(-\zeta_i\zeta_j S_{ij})$. Therefore, the conceptual picture that orthogonality of ω and ζ promotes area production is not inconsistent with the equations, but clearly is an oversimplification as it does not consider the coupling of ω and ζ with strain.

5. Alignment of mass fraction gradients, vorticity and strain

Because according to Eq. (23) the orthogonality of ω and ζ has a substantial effect on $(-\zeta_i\zeta_j S_{ij})$, the PDF of $\cos(\omega,\zeta)$ is shown in Fig. 22. For all layers, the PDF exhibits a maximum for $\cos(\omega,\zeta)=0$, i.e., for the vectors being perpendicular, similar to the findings of Ruetsch and Ferziger,[15] although their results were obtained for the mixture fraction computed as a passive scalar in incompressible homogeneous turbulence. All PDFs have a similar peak magnitude, with the exception of the HN800 layer whose peak is considerably higher, which coincides with the larger activity in area production found from Fig. 12. However, in Fig. 20, the HN800 layer also had the largest planar average and RMS values of $(\omega\cdot\zeta)$ (i.e., nonorthogonal activity). Thus, we could not confirm the hypothesis of Ruetsch and Ferziger[15] that the orthogonality of ω and ζ leads to maximal area production, although the circumstantial evidence appears to support this hypothesis.

Finally, we inquire whether ω and ζ show a tendency to align with the principal strain directions, by performing an analysis similar to that of Ashurst *et al.*[19] Here, the principal strain rates (strain matrix eigenvalues) are ordered as $\epsilon_1 \leqslant \epsilon_2 \leqslant \epsilon_3$ and the (unit) eigenvector corresponding to ϵ_i is denoted σ_i (the σ_i vectors are orthogonal.). The first invariant of the strain matrix is $I_1 = S_{kk} = \epsilon_1 + \epsilon_2 + \epsilon_3$. In contrast to the incompressible case where $S_{kk}=0$, $\epsilon_1 \leqslant 0$ and $\epsilon_3 \geqslant 0$, in the present situation $\epsilon_1+\epsilon_2+\epsilon_3 \neq 0$; however, ϵ_1 was found to be almost exclusively negative whereas ϵ_3 was almost exclusively positive, which is similar to the incompressible situation. For all layers, ϵ_2 is about twice as likely to be positive than negative, with 61%–67% of the points in the domain having positive ϵ_2 and the OH500 and OH550 layers having higher likelihood of positive ϵ_2. Therefore, it seems more likely for the flow to be stretched in the second eigenvector direction. Since the orientation of the σ_i is arbitrary, the signs of $\cos(\sigma_i,\omega)$ and $\cos(\sigma_i,\zeta)$ are not significant, and therefore only their magnitude is here analyzed. The PDFs of $\cos(\sigma_i,\omega)$ and $\cos(\sigma_i,\zeta)$, calculated by considering only the points within the layer $(0.005 \leqslant Y_2 \leqslant 0.995)$, are presented in Fig. 23. Clearly, ω is most likely to be aligned with σ_2 (similar to the low-pressure numerical results of Kosović *et al.*[20] and the experimental results of Tao *et al.*[21,22]) whereas ζ is most likely to be orthogonal with σ_2, consistent with the previous finding in Fig. 22 that ω and ζ are most likely to be orthogonal. On the other hand, although ζ is more likely to be parallel to σ_1 than to σ_3 (except for the OH750 layer), the most likely orientation is parallel to σ_1 for the HN layers but at about 41° to σ_1 for the OH layers. Noteworthy, the HN800 $\cos(\sigma_1,\zeta)$ PDF has two peaks (46° and 0°) whereas all the other layers have only one peak. For all layers, the $\cos(\sigma_3,\zeta)$ PDF exhibits a peak around 0.65 (49°), although the peak is very shallow for HN500 and HN600. Thus, it seems that the flow is most likely to be stretched in the direction of preferential ω alignment that is also the preferential direction of ζ orthogonality. This analysis reveals that the aspect of the HN800 PDFs is much closer to that of the OH layers than the other HN layers, consistent with the smoother features common to OH and HN800 layers.

Therefore, whereas perpendicular (ω,ζ) and parallel (ω,σ_2) seems to be the most likely alignment for all supercritical layers, the most likely orientation of ζ with respect to strain shows quite some variability depending on species system and initial conditions. The preferential alignment of ω and σ_2 casts doubts on the use of eddy-viscosity-type subgrid models for large eddy simulation in adequately predicting the turbulent mixing of supercritical fluids.

IV. SUMMARY AND CONCLUSIONS

Databases obtained from direct numerical simulations of binary-species supercritical temporal mixing layers were compared to investigate the species-dependent aspects of supercritical turbulence. Simulations were performed for O_2-H_2 and $C_7H_{16}-N_2$ layers, at approximately the same reduced pressure of 2 with respect to the pure heavier species and similar momentum ratios. The O_2-H_2 mixture was asymptotically close to ideal, whereas the $C_7H_{16}-N_2$ mixture experienced strong departures from ideality. Each layer had the heavier species in the lower stream and the lighter spe-

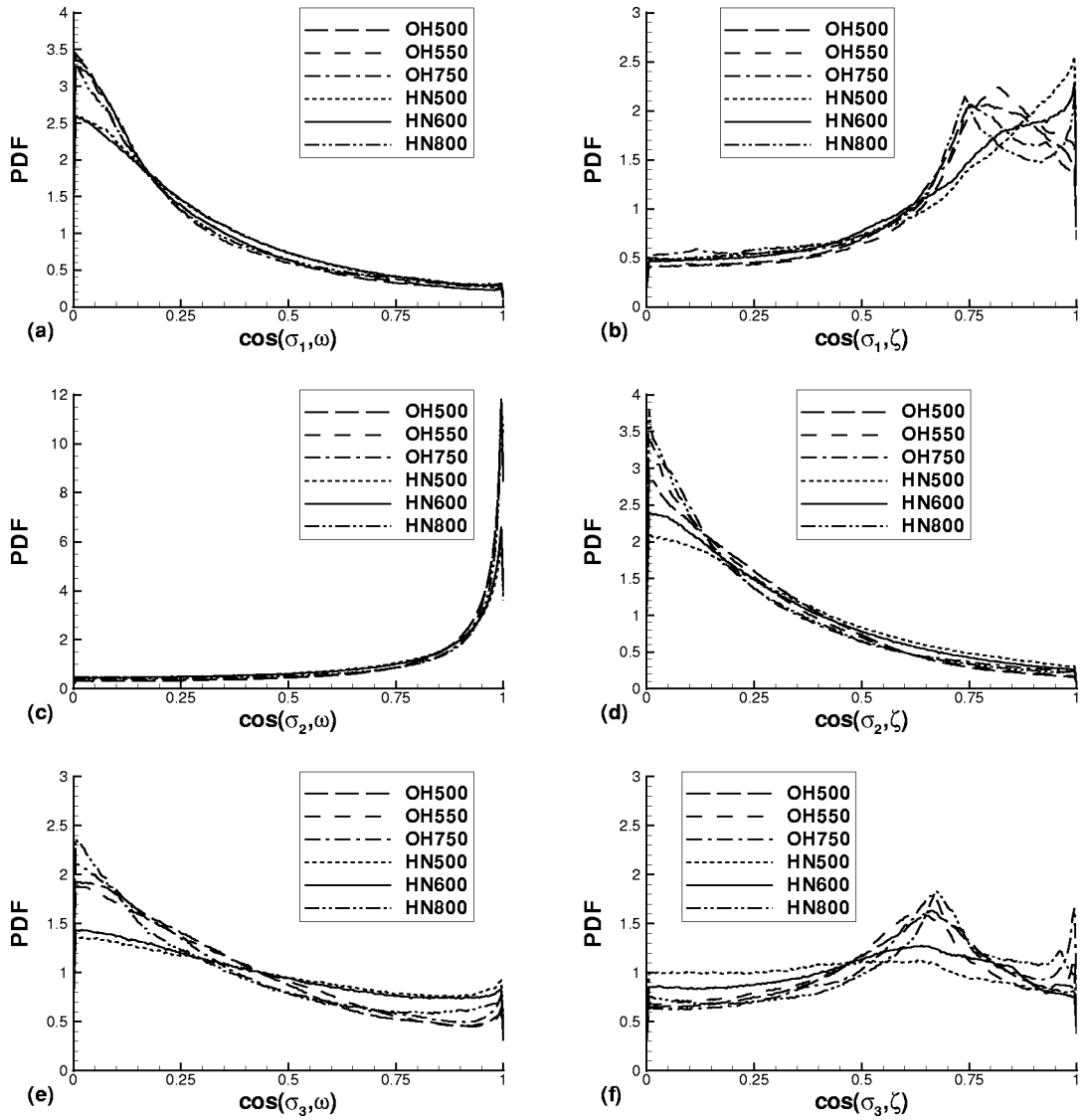

FIG. 23. Probability density function of (a), (c), and (e) $\cos(\sigma_i,\omega)$ and (b), (d), and (f) $\cos(\sigma_i,\zeta)$ at the respective transitional states for all layers listed in Table IV. For points within the layer $(0.005 \leqslant Y_2 \leqslant 0.995)$.

cies in the upper stream, and was initially perturbed to initiate entrainment, roll-up and pairing so that it eventually reached a transitional state. The database used in this study consisted of three simulations each of the O_2-H_2 and the $C_7H_{16}-N_2$ layer, and the initial conditions for the same binary species system differed by the initial vorticity-thickness-based Reynolds number, the initial-perturbation wavelength and the amplitude of the spanwise initial perturbation.

Global characteristics of the six layers showed that the momentum thickness and product thickness growth is substantially reduced for the O_2-H_2 layers compared to the $C_7H_{16}-N_2$ ones, and that the levels of the positive spanwise vorticity and the enstrophy for the O_2-H_2 layers were also diminished, indicating less turbulence activity. These results are attributed to the much larger initial density stratification of the O_2-H_2 layers, which delays entrainment and pairing.

All layers displayed high density-gradient magnitude regions at transition, which form due both to the distortion of the initial density stratification boundary and to the mixing of the species, and all layers exhibited high mass-fraction gradient regions. For $C_7H_{16}-N_2$ and O_2-H_2 layers having the same initial perturbations and momentum-thickness based Reynolds numbers at transition, these regions are stronger but narrower for $C_7H_{16}-N_2$; this behavior was here attributed to the reduced solubility and mixture non-ideality when compared to the O_2-H_2 system. Most of the dissipation (irreversible entropy production) activity occurred in these high density-gradient magnitude and high mass-fraction gradient regions; however, the largest dissipation is located for the O_2-H_2 layers within regions originating from the distortion of the original density stratification boundary, and for the $C_7H_{16}-N_2$ layers within regions created through mixing. The maximum dissipation level is larger for the O_2-H_2 layer, consistent with the lower turbulence levels detected from the global analysis. For all layers, the dissipation at transition was dominated by the contribution from the species-mass flux, with the contribution from viscous and thermal effects

being much smaller. Thus, for supercritical mixing layers, we identified structures (high density-gradient and high mass-fraction-gradient regions) and thermodynamic processes (solubility and mixture ideality) that affect turbulence development.

Directly related to fluid disintegration, the area production of fluid fronts perpendicular to the mass fraction gradient was examined in a coordinate system moving with the relative velocity between the front and the flow. Smaller wavelength initial perturbations combined with larger initial vorticity-thickness based Reynolds numbers led to enlarged area creation, suggesting a possible strategy for the control of area production. Area production for $C_7H_{16}-N_2$ layers was found to be larger than for the O_2-H_2 layers, this being attributed to the smaller initial density stratification of the $C_7H_{16}-N_2$ layers as well as to the manifestation of the strong pressure–density coupling through the equation of state, resulting from considerable departures from perfect gas and ideal mixture behavior. This coupling manifested itself through greater coincidence of regions of significant magnitude of the pressure and density gradients. These findings highlight the importance of real gas thermodynamics in the modeling of supercritical turbulent mixing. The distribution of the strain–mass-fraction-gradient alignment differed among the layers, but calculations of the vorticity–mass-fraction-gradient alignment found orthogonality to be the most likely orientation. The layer with the largest fluid-front area production also had the highest probability of orthogonal vorticity and mass-fraction gradients. These results were not directly obvious from the budgets of various terms contributing to the area production, since orthogonality between vorticity and mass-fraction gradient reduces both the numerator and the denominator of a ratio involved in the calculation of the area production. Thus, the simple interpretation of Ruetsch and Ferziger[15] regarding the role of vorticity and mass fraction gradient orthogonality promoting area production could not be directly confirmed here; rather the evidence is of circumstantial nature. Finally, the finding that the vorticity is aligned with the intermediate strain-rate direction indicates that the use of eddy-viscosity-type subgrid models for large eddy simulation is inadequate in predicting turbulent mixing under supercritical conditions.

ACKNOWLEDGMENTS

This work was conducted at the Jet Propulsion Laboratory (JPL), California Institute of Technology (Caltech) and sponsored by the National Aeronautics and Space Administration (NASA), Marshall Space Flight Center under the direction of Dr. John Hutt, by the Air Force Office of Scientific Research under the direction of Dr. Julian Tishkoff, and by the Army Research Office under the direction of Dr. David Mann, through interagency agreements with NASA. The computational resources were provided by the JPL Supercomputing Center. One of the authors (J.B.) would like to thank Professor Dale Pullin of Caltech for bringing Ref. 15 to her attention.

[1] J. Prausnitz, R. Lichtenthaler, and E. de Azevedo, *Molecular Thermodynamics for Fluid-Phase Equilibrium* (Prentice-Hall, Englewood Cliffs, NJ, 1986).
[2] J. Hirshfelder, C. Curtis, and R. Bird, *Molecular Theory of Gases and Liquids* (Wiley, New York, 1964).
[3] K. Harstad and J. Bellan, "Evaluation of commonly used assumptions for isolated and cluster heptane drops in nitrogen at all pressures," Combust. Flame **127**, 1861 (2001).
[4] T. Clifford, *Fundamentals of Supercritical Fluids* (Oxford University Press, New York, 1999).
[5] B. Chehroudi, D. Talley, and E. Coy, "Initial growth rate and visual characteristics of a round jet into a sub- to supercritical environment of relevance to rocket, gas turbine and diesel engines," AIAA Pap. 99-0206 (1999); AIAA Thirty-Seventh Aerospace Sciences Meeting and Exhibit, Reno, NV, January 11–14.
[6] W. Mayer, A. Schik, C. Schweitzer, and M. Schaffler, "Injection and mixing processes in high pressure LOX/GH2 rocket combustors," AIAA Pap. 96-2620 (1996); AIAA/ASME/SAE/ASEE Thirty-Second Joint Propulsion Conference, Lake Buena Vista, FL, July 1–3.
[7] W. Mayer, B. Ivancic, A. Schik, and U. Hornung, "Propellant atomization in LOX/GH2 rocket combustors," AIAA Pap. 98-3685 (1998); AIAA/ASME/SAE/ASEE Thirty-Fourth Joint Propulsion Conference and Exhibit, Cleveland, OH, July 13–15.
[8] M. Oschwald and A. Schik, "Supercritical nitrogen free jet investigated by spontaneous Raman scattering," Exp. Fluids **27**, 497 (1999).
[9] R. Miller, K. Harstad, and J. Bellan, "Direct numerical simulations of supercritical fluid mixing layers applied to heptane-nitrogen," J. Fluid Mech. **436**, 1 (2001).
[10] N. Okong'o and J. Bellan, "Direct numerical simulation of a transitional supercritical binary mixing layer: Heptane and nitrogen," J. Fluid Mech. **464**, 1 (2002).
[11] N. Okong'o, K. Harstad, and J. Bellan, "Direct numerical simulations of O_2/H_2 temporal mixing layers under supercritical conditions," AIAA J. **40**, 914 (2002).
[12] I. Hannoun, H. Fernando, and E. List, "Turbulence structure near a sharp density interface," J. Fluid Mech. **189**, 189 (1988).
[13] D. Briggs, J. Ferziger, J. Koseff, and S. Monismith, "Turbulent mixing in a shear-free stably stratified two-layer fluid," J. Fluid Mech. **354**, 175 (1998).
[14] J. Bellan, "Supercritical (and subcritical) fluid behavior and modeling: Drops, streams, shear and mixing layers, jets and sprays," Prog. Energy Combust. Sci. **26**, 329 (2000).
[15] G. Ruetsch and J. Ferziger, "Effects of small-scale structure on turbulent mixing," Center for Turbulence Research Annual Research Briefs 213–235 (1997).
[16] M. Matalon, "On flame stretch," Combust. Sci. Technol. **31**, 169 (1983).
[17] S. Chung and C. Law, "An invariant derivation of flame stretch," Combust. Flame **55**, 123 (1984).
[18] S. Candel and T. Poinsot, "Flame stretch and the balance equation for the flame area," Combust. Sci. Technol. **70**, 1 (1990).
[19] W. Ashurst, A. Kerstein, R. Kerr, and C. Gibson, "Alignment of vorticity and scalar gradient with strain rate in simulated Navier–Stokes turbulence," Phys. Fluids **30**, 2343 (1987).
[20] B. Kosović, D. I. Pullin, and R. Samtaney, "Subgrid-scale modeling for large-eddy simulations of compressible turbulence," Phys. Fluids **14**, 1511 (2002).
[21] B. Tao, J. Katz, and C. Meneveau, "Geometry and scale relationships in high Reynolds number turbulence determined from three-dimensional holographic velocimetry," Phys. Fluids **12**, 941 (2000).
[22] B. Tao, J. Katz, and C. Meneveau, "Statistical geometry of subgrid-scale stresses determined from holographic particle image velocimetry measurements," J. Fluid Mech. **457**, 35 (2002).
[23] P. J. Diamessis and K. K. Nomura, "Interaction of vorticity, rate-of-strain, and scalar gradient in stratified homogeneous sheared turbulence," Phys. Fluids **12**, 1166 (2000).
[24] J. Bellan and K. Harstad, "An all-pressure fluid-drop model: Validation and species system dependency," (2002); JANNAF Meeting, Destin, Florida, April 8–12, 2002.
[25] N. Okong'o and J. Bellan, "Real gas effects on mean flow and temporal, inviscid linear stability of binary-species mixing layers," AIAA J. **41**, 2429 (2003).
[26] J. Keizer, *Statistical Thermodynamics of Nonequilibrium Processes* (Springer-Verlag, New York, 1987).

[27]S. Sarman and D. Evans, ''Heat flux and mass diffusion in binary Lennard-Jones mixtures,'' Phys. Rev. A **45**, 2370 (1992).
[28]K. Harstad and J. Bellan, ''An all-pressure fluid-drop model applied to a binary mixture: Heptane in nitrogen,'' Int. J. Multiphase Flow **26**, 1675 (2000).
[29]K. Harstad, R. Miller, and J. Bellan, ''Efficient high pressure state equations,'' AIChE J. **43**, 1605 (1997).
[30]K. Harstad and J. Bellan, ''Isolated fluid oxygen drop behavior in fluid hydrogen at rocket chamber pressures,'' Int. J. Heat Mass Transfer **41**, 3537 (1998).
[31]K. Harstad and J. Bellan, ''The D^2 Variation for isolated LOX drops and polydisperse clusters in hydrogen at high temperature and pressures,'' Combust. Flame **124**, 535 (2001).
[32]D. Papamoschou and A. Roshko, ''The compressible turbulent shear layer: An experimental study,'' J. Fluid Mech. **197**, 453 (1988).
[33]R. Moser and M. Rogers, ''Mixing transition and the cascade to small scales in a plane mixing layer,'' Phys. Fluids A **3**, 1128 (1991).
[34]R. Moser and M. Rogers, ''The three-dimensional evolution of a plane mixing layer: Pairing and transition to turbulence,'' J. Fluid Mech. **247**, 275 (1993).
[35]N. Okong'o and J. Bellan, ''Consistent boundary conditions for multicomponent real gas mixtures based on characteristic waves,'' J. Comput. Phys. **176**, 330 (2002).
[36]C. Kennedy and M. Carpenter, ''Several new numerical methods for compressible shear layer simulations,'' Appl. Numer. Math. **14**, 397 (1994).
[37]S. M. Muller and D. Scheerer, ''A method to parallelize tridiagonal solvers,'' Parallel Comput. **17**, 181 (1991).
[38]A. Cortesi, B. Smith, G. Yadigaroglu, and S. Banerjee, ''Numerical investigation of the entrainment and mixing processes in neutral and stably-stratified mixing layers,'' Phys. Fluids **11**, 162 (1999).
[39]N. Okong'o and J. Bellan, ''Entropy production of emerging turbulent scales in a temporal supercritical n-heptane–nitrogen three-dimensional mixing layer,'' Proc. Combust. Inst. **28**, 497 (2000).
[40]Z. She, E. Jackson, and S. Orszag, ''Structure and dynamics of homogeneous turbulence-models and simulations,'' Proc. R. Soc. London, Ser. A **434**, 101 (1991).
[41]K. Ohkitani and S. Kishiba, ''Nonlocal nature of vortex stretching in an inviscid fluid,'' Phys. Fluids **7**, 411 (1995).
[42]K. Nomura and G. Post, ''The structure and dynamics of vorticity and rate of strain in incompressible homogeneous turbulence,'' J. Fluid Mech. **377**, 65 (1998).